Iowa State University
Digital Repository

2012

Detector response calibration for the NOvA quasi-elastic cross-section measurement

Timothy David Kutnink
Iowa State University

Follow this and additional works at: http://lib.dr.iastate.edu/etd

Part of the Physics Commons

Detector response calibration for the NOνA quasi-elastic cross-section measurement

by

Timothy David Kutnink

A thesis submitted to the graduate faculty

in partial fulfillment of the requirements for the degree of

MASTER OF SCIENCE

Major: High Energy Physics

Program of Study Committee:

Mayly Sanchez, Major Professor

James Cochran

Kevin de Laplante

Marzia Rosati

Iowa State University

Ames, Iowa

2012

DEDICATION

I would like to dedicate this thesis to my mother, Vanessa Kutnink, for her love and the inspiration for me to go into Physics and accomplish this work. Also, my friends and family for their love and support.

TABLE OF CONTENTS

LIST OF TABLES

LIST OF FIGURES

ACKNOWLEDGEMENTS

ABSTRACT

NOνA is a long-baseline neutrino experiment designed to observe the neutrino oscillation phenomenon of muon neutrinos oscillating into electron neutrinos. The NuMI beam line located at Fermilab produces the muon neutrinos for this observation. The Near and Far Detectors are constructed off-axis of the NuMI beam line and located at Fermilab and northern Minnesota (electron neutrino appearance maximum), respectively. In order to carry out the long-term goals of the experiment, the NOνA Near Detector Prototype (NDOS) was built and commissioned at Fermilab. Its goals are to demonstrate that, using the same materials and technologies as the larger NOνA detectors, we are able to observe neutrino data from the NuMI beam and cosmic ray muons. The cosmic ray muon data were used in the commissioning and it is currently being used in testing of detector response. These data are also being used in the development of reconstruction and calibration techniques to be used in the Near and Far Detectors. Furthermore, the neutrino data acquired are being used in the development and implementation of physics analyses, not only for NDOS data, but also for the first NOνA data. This thesis will discuss the development of the detector response calibration using cosmic ray muon data and its effects on the preliminary charged current quasi-elastic cross-section measurement using beam neutrino data in the NDOS.

CHAPTER 1.   The NOνA Experiment

NOνA (NuMI[†] Off-axis ν_e Appearance) is a long-baseline neutrino experiment designed to observe electron neutrino appearance in a muon neutrino beam. The NOνA detectors are specifically designed to identify electron neutrino interactions and provide excellent background rejection of other interactions with an electromagnetic shower component. NOνA's primary goals are to measure the neutrino mixing angle θ_{13}, determine the mass hierarchy (the sign of Δm_{13}^2), and provide insight into the CP violating phase term, δ_{CP}. The NOνA collaboration would like to perform a more precise measurement of θ_{23} and Δm_{32}^2.

An important aspect of long-baseline neutrino experiments is their use two detectors in order to make more precise measurements. The placement of one detector near the source of the neutrinos, for NOνA it is the NuMI beam at Fermilab, allows for the study of the flux of neutrinos coming from that source. This information can then be extrapolated for an estimate of the expected numbers and energies of oscillated neutrinos seen in the Far Detector. The Far Detector is situated 810 km from the source in Ash River, Minnesota, near an oscillation maximum so that the number of neutrinos observed changing flavor is largest. The NOνA detectors are designed to be functionally identical in order to reduce many systematic uncertainties associated with the measurements. The two detector design allows these uncertainties to cancel out between detectors in turn producing a more precise measurement. They are also designed to be fully active detectors. Thus, in addition to the detector mass being available for neutrinos to interact, the outgoing charged particles can be detected by greater than 70% of the detector mass. The physical dimensions of the Near Detector are 4.1 m wide and 4.1 m tall and 14.5 m in length, also weighing 330 tons. For the Far Detector, it is 15.5 m in width and height, and 59.8 m in length, weighing just over 14 ktons.

[†]Neutrinos at the Main Injector.

The NOνA detector design has not been used in previous experiments. Therefore a prototype detector called the NDOS† has been built to test all elements of the detector. The goal of this prototype is to demonstrate that the technologies are scalable to a large deployment such as the one required on NOνA. Also, by using the NDOS exposure to cosmic ray muons and neutrinos from the NuMI beam we developed the simulation, reconstruction and calibration to be used in the physics analyses of the NOνA experiment. Finally, we can use muon neutrino charged current quasi-elastic interactions to make a first measurement of this neutrino-nucleus cross-section with the NOνA detectors.

1.1   NuMI Neutrino Beam

NOνA will detect neutrinos from the NuMI (Neutrinos at the Main Injector) beam at the Fermi National Accelerator Laboratory (Fermilab) in Batavia, IL. Following Figure 1.1 we start near the point indicated Linac and Booster, exactly starting at the large red dot. The process of creating a neutrino beam begins by feeding protons (produced from ionizing hydrogen) into an accelerator that increases their energy. A Cockcroft-Walton generator starts the acceleration, the large red dot in Figure 1.1, of the proton to be fed into the linear accelerator, which is connected to the Booster ring and finally the Main Injector ring (right before the Tevatron Ring). Once in the Main Injector ring, the protons are diverted into a target hall, where they collide with a graphite target to produce large amounts of charged pions and kaons. The target consists of forty-seven 2 cm long segments with 0.3 mm spacing between the segments. The segments are 6.4 mm wide and 15 mm high [1]. The intensity of the beam and exposure of the detectors to the beam is measured as a function of the number of protons on target (POT). A typical POT exposure per spill is about 10^{13} POTs and NOνA is expected to accumulate 3×10^{20} POTs per year. Figure 1.2 shows the Target Hall coming off the Main Injector. The NDOS is located between the Muon Alcoves and the Near Detector Hall but at ground level near the Surface Building. This puts the NDOS at 6.3° or 110 mrad off-axis of the NuMI beam line [2].

Pions and kaons produced from the proton collision are sent through a set of magnetic horns

---

†Near Detector On the Surface.

Figure 1.1: An aerial photograph of the accelerating rings and neutrino beams at Fermilab. Courtesy of Fermi National Accelerator Laboratory.

which have a dual purpose. The first goal is to focus the charged particles into an intense beam. The second purpose is to select which type of beam is desired, either neutrino or anti-neutrino beam. The schematic of the focusing system is shown in Figure 1.3 which displays a section of the horns indicating the direction of the current on the horn to generate the required magnetic field to focus positively charged pions and kaons.
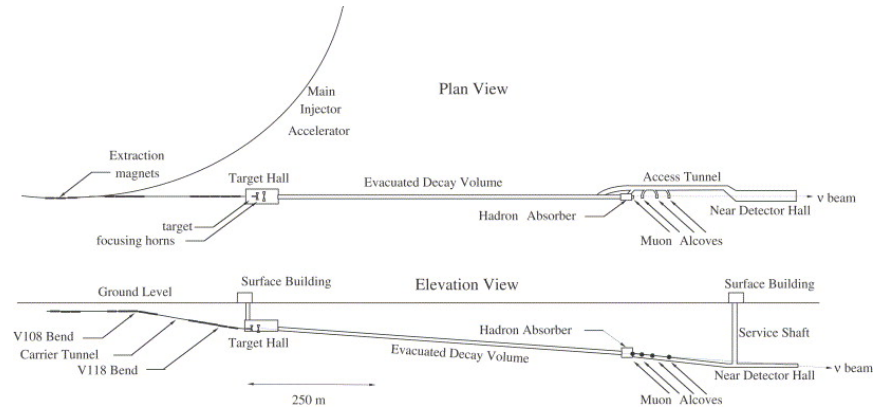
Figure 1.2: A schematic representation of the NuMI target hall off of the Main Injector [3]. This shows where the muons will decay producing the muon neutrino beam. The NDOS building is at ground level near the Surface Building above the Near Detector Hall closer to the Target Hall.
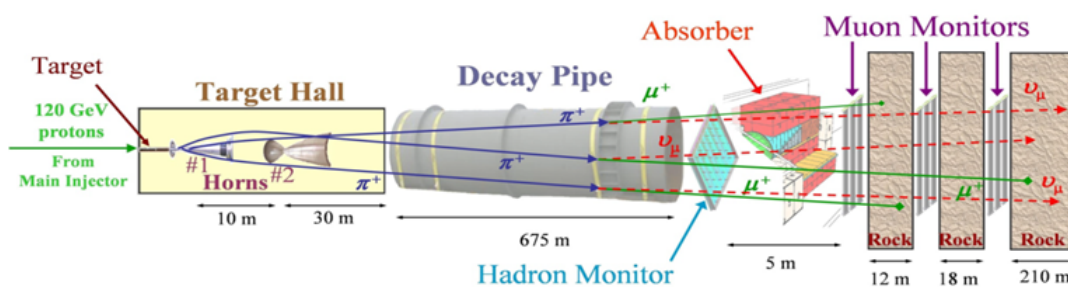
Figure 1.3: A schematic representation of the NuMI target, the focusing horns, and the decay tunnel.

The charged pions will decay to muons and muon-neutrinos 99.99% of the time and charged kaons will decay to muons and muon-neutrino 63.55% of the time [4]. When the pion (kaon) decays, the muon neutrino is likely to be boosted in the same direction of the decayed pion, creating the muon neutrino beam. Since the sign of the current of the magnetic horns can be

chosen, the direction of the magnetic field can be changed which can preferentially select the charge of particles going through the horn by deflecting one charge and focusing the opposite charge, and thus the type of beam. The pions and kaons decay into muons and neutrinos as they travel along an evacuated tunnel approximately 700 m in length. The pion and kaon lifetimes are 26 ns and 12.4 ns respectively. Muons have longer mean lifetimes, 2.2 μs, thus propagate without decaying for a longer distance so they tend to decay at the end of the tunnel. To prevent hadron (pion, kaon) and muon contamination crossing the Near Detector, rock and concrete remain between the end of the tunnel and the detector to act as an absorber material. The particle decay processes that contribute to the beam of neutrinos are:

$$\pi^+ \rightarrow \mu^+ + \nu_\mu$$
$$K^+ \rightarrow \mu^+ + \nu_\mu$$

$$(1.1)$$

A small amount of anti-neutrino contamination is expected from high energy π^- and K^- that do not get deflected by the magnetic horns. The decays involved are:

$$\pi^- \rightarrow \mu^- + \bar{\nu}_\mu$$
$$K^- \rightarrow \mu^- + \bar{\nu}_\mu$$

$$(1.2)$$
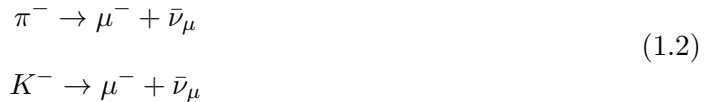
Finally some of the resulting muons will eventually decay and create background neutrinos to the beam:

$$\mu^+ \rightarrow e^+ + \bar{\nu}_\mu + \nu_e$$
$$\mu^- \rightarrow e^- + \nu_\mu + \bar{\nu}_e$$

$$(1.3)$$

The source of the neutrinos for NOνA is the NuMI beam. NOνA places the detectors off-axis of the NuMI beam direction to control the energy peak and range of the neutrinos produced from the NuMI beam. Figure 1.4 shows the energy spectra distributions for different off-axis angles at 810 km from the source. By moving the detector off-axis the energy spectrum becomes narrower with lower neutrino energy. The NOνA detectors will be constructed 14 mrad off-axis of the NuMI beam direction so that the energy peak is at the first oscillation maximum.

At the NDOS location, 110 mrad off-axis, the detector instead sees two distinct energy peaks, shown in Figure 1.5. The first energy peak is produced predominantly from pion decays in the beam line and the second energy peak, which is the energy that NOνA is most interested in, comes predominantly from kaon decays. The NDOS collected NuMI events from December 2010 to March 2012 for a total of 3×10^{20} POTs as shown in Figure 1.6.
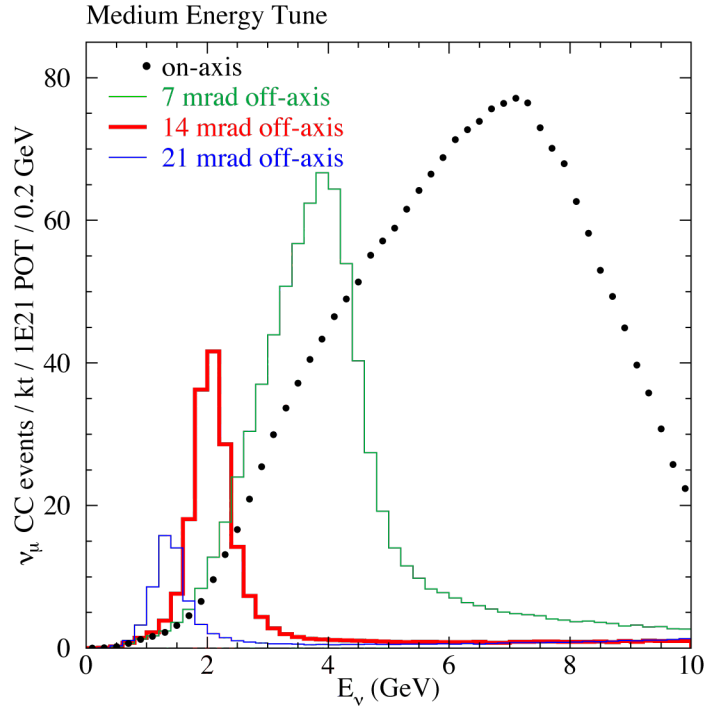
Figure 1.4: This shows the expected number of neutrinos as a function of energy at varying angles with respect to the beam axis. This shows as a detector is moved further off the beam axis the peak energy of the beam decreases but the range becomes smaller as well. This allows for using a well defined energy spectrum to answer neutrino physics problems.

1.2 NOνA Near Detector Prototype

The Near Detector Prototype (NDOS - Near Detector On the Surface), shown in Figure 1.7 was built to help the overall experiment in achieving the scientific endeavors and contributions that has been laid out by the NOνA collaboration. The goals of the NDOS are to test the assembly techniques that will be used at the Near and Far Detector construction sites; to install, operate and test the NOνA electronics and data acquisition, as well as to develop
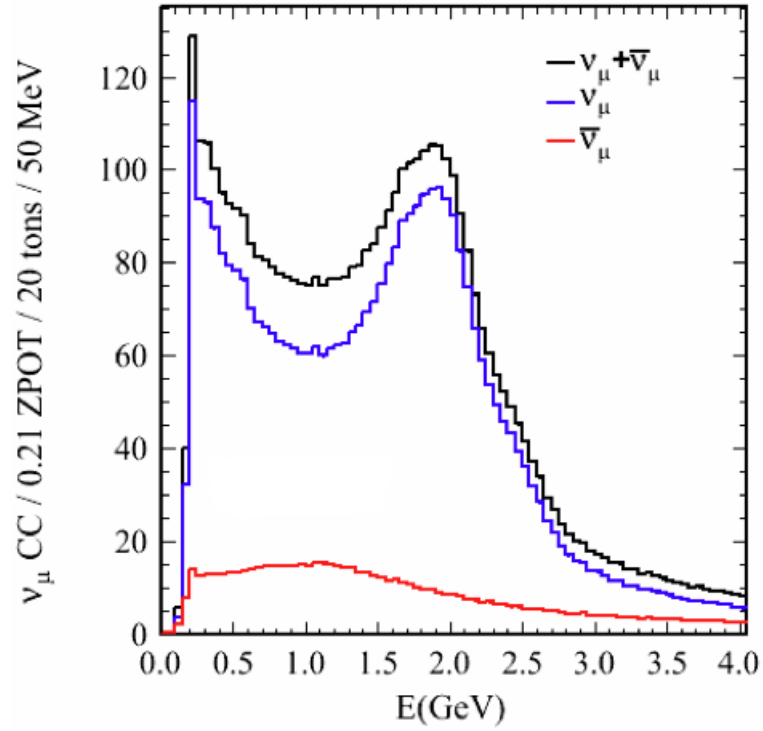
Figure 1.5: The distribution of the number of charged current muon neutrino events per 0.21×10^{21} POTs per 20 tons of detector mass per 50 MeV of neutrino energy. The first peak corresponds to most of the pion decays in the beam, whereas the second peak corresponds to the kaon decays. This was for the neutrino (forward horn current) beam configuration [5].
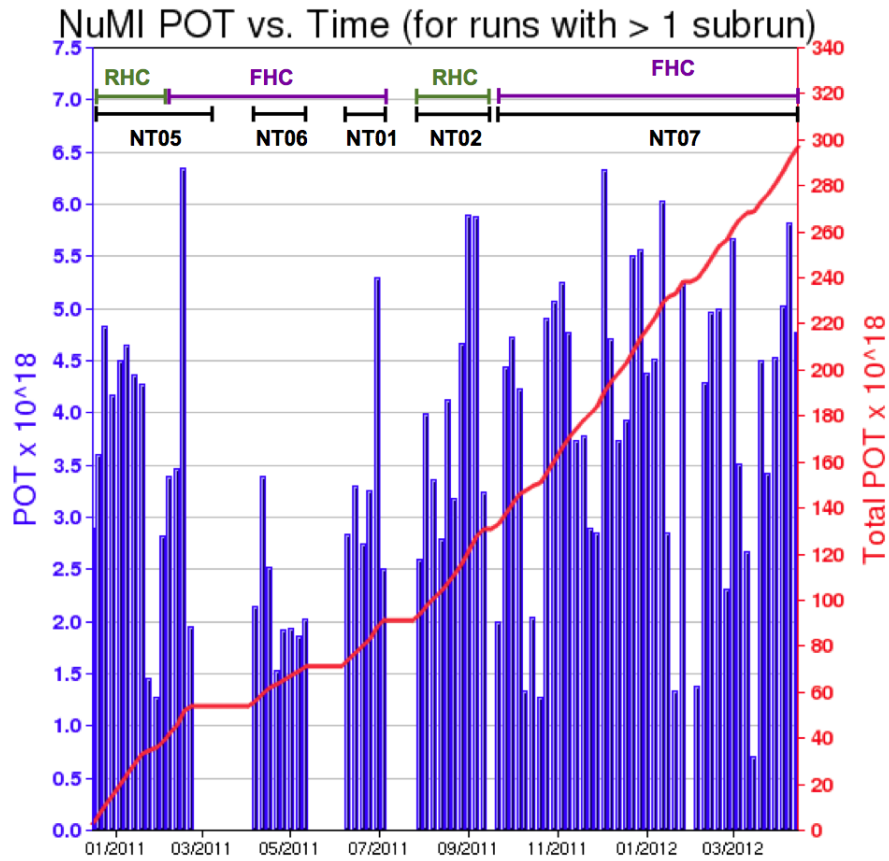
Figure 1.6: This distribution shows the number of delivered POTs from NuMI during the time NDOS was taking neutrino data. The spaces where no POTs were delivered are due to shutdowns and replacements of the targets. The targets used are indicated by the black spanning lines and NT0# code. The green spanning line shows the period when the beam was an anti-neutrino beam with the reverse horn current (RHC) applied. The violet spanning line shows the period when the beam was a neutrino beam with the forward horn current (FHC) applied [6].

Figure 1.7: The fully constructed NDOS at Fermilab in the surface building. This shows the NDOS from the muon catcher (back) end of the detector. A physicist stands beside the detector during commissioning and shows the relative size of the detector.

the reconstruction and calibration methods that will be later used on the physics analyses incorporating all the detectors. In this section I will give a general description of the NDOS then discuss the material and technologies used in the NDOS that will later be used in the Near and Far Detectors. Finally, I will describe the capabilities and observed performance of the NDOS.

The detector is situated in a surface building close to the construction site of the future underground Near Detector. The NDOS was built during 2010 and its physical dimensions are 2.8 m wide by 4.1 m tall by 14.5 m in length. We started taking data with this 222-ton detector in December 2010. It uses the same materials and technologies that the NOνA Near and Far Detectors will use, thus allowing us to test and prepare for the larger scale construction. The detectors are constructed from rigid PVC extruded into rectangular cells filled with liquid scintillator. Figure 1.8 shows where and how the light signal generated by a charged particle in a detector cell is processed. A wavelength shifting fiber is strung through the cell in a U shape with both ends of the fiber coming out one side of the cell that will pick up the light from the charged particle. This cell along with 31 other cells form one module that string the
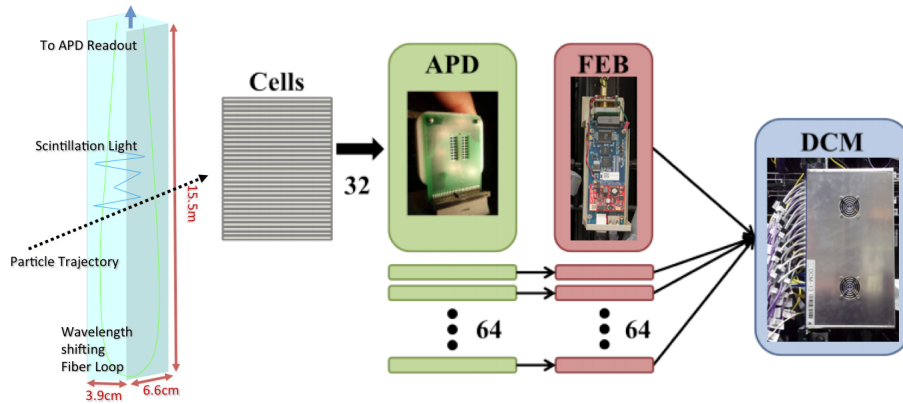
Figure 1.8: This shows the process whereby a charged particle generates light in the liquid scintillator, with the wavelength shifting fiber transmitting the signal to an avalanche photo-diode. A total of 32 cells are attached to the avalanche photodiode and the front end board takes that signal and processes it. It then sends the processed signal to the data concentrator module where it is synchronized with the signals of a total of 64 front end board and is then sent to computers for storage and later analysis.

fibers through a manifold to be read out by a photodetector. This photodetector, an avalanche photodiode, is attached to a front end board that processes the electric signal and sends it to computers for storage and later analysis.

The NDOS also has a muon catcher, which is 11 planes of liquid scintillator sandwiched between steel plates in order to better contain muon tracks. The steel plates of the muon catcher are 2.9 m wide by 4.1 m tall and 0.1 m thick, each weighing 8.2 metric tons. The muon catcher is necessary because 1-2 GeV muons produced by neutrinos in the beam can traverse and exit the length of the detector. These muons will lose more energy within the muon catcher due to the higher density of the steel.

Most of the technology and materials used in constructing the NOνA detectors have not been used in such a large scale operation. This makes the NDOS an important step in the overall NOνA experiment. These items will be discussed in further detail in sections below.

1.2.1 PVC Extrusions

The bulk structure of the NDOS and also the other NOνA detectors comprises of rigid polyvinyl chloride (rigid PVC) extruded into singular casts of 16 cellular cavities (cell), made

by Extrutech, in which two of these extrusions are glued together to create one module, together with an end cap at one end and a fiber manifold for bundling the fibers at the other. Figure 1.9 shows a schematic of the construction of one module. The dimensions of the extrusion in the NDOS are 6.5 cm wide and 63.5 cm in height, and depending on orientation in the detector, approximately 2.6 m in length for horizontally placed extrusions and approximately 3.9 m in length for verticals. Two vertical modules glued together create an x-view plane (a plane that specifies the x-coordinate of a charged particle track) and three horizontal modules glued together create the y-view plane (specifying the y-coordinate) for the NDOS. The PVC is loaded with higher than normal amounts of titanium dioxide (TiO_2) than commercial products for the purpose of having a higher reflectivity of light generated in the cell from the scintillator. We use TiO_2 for higher reflectivity efficiency in shorter wavelengths and higher light yields obtained at the photodetectors. The purpose of the reflectivity is to enhance light collection, since light generated in the liquid scintillator may not travel directly to the wavelength shifting fiber. It is calculated on average that the light reflects 10 times before entering the fiber to then be read out. The fiber manifold at one end of the two extrusions is a black injection-molded plastic designed to bundle the two ends of wavelength shifting fibers from each cell to be connected directly to the APD for readout. This region of the manifold is referred to as the snout.

Cracks formed on the manifolds during and after transport of the NDOS modules to Fermilab. A method for finding cracks and fixing them on the NDOS was implemented, while a new pressure test for the manifolds was developed. No cracks have been reported on the Far Detector construction. The initial mixture of PVC used for the NDOS is not completely light tight from ambient light sources. Exposed PVC surfaces needed to be painted black as a measure to reduce unanticipated noise from those light sources.

1.2.2 Liquid Scintillator

The PVC extrusions are filled with liquid scintillator as a means to generate the light produced by charged particles from the different interaction $NO\nu A$ is interested in studying. The liquid scintillator is a mixture of pseudocumene (4.1% by weight) in mineral oil (95.8% by weight) blended with some powder wavelength shifters (PWS), an anti-static additive, and an
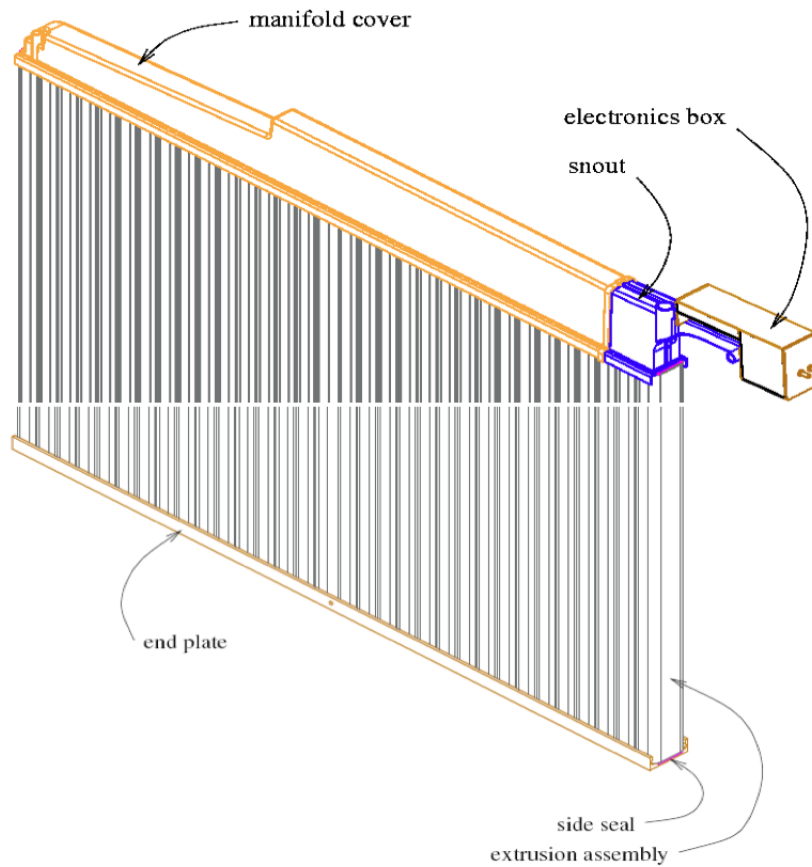
Figure 1.9: A schematic drawing of the module used in all NOνA detectors from an angled perspective and is truncated (white line) to show both ends. This has two 16 cell extrusions (grey) glued together to form a single module, fibers fed through each cell and their ends are bundled in the manifold (orange). They are subsequently guided in the snout (blue).

antioxidant (0.1% combined by weight). The light generation in the scintillator results from charged particles traversing through the scintillator, exciting the psuedocumene, and then radiating a photon in the ultraviolet (UV) spectrum. The light has its wavelength doubly shifted by an amount such that the reflectivity efficiency is highest in the PVC. The pseudocumene radiates at a peak about 290 nm in the UV, the first PWS absorbs most of the pseudocumene radiation range and emits at a peak around 360 nm in the UV, where again the second PWS absorbs most of that emitted radiation and emits itself at about 420 nm in the visible spectrum of light. The antioxidant reduces the oxygenation levels and removes radicals from the scintillator as these causes a drop in light yield from scintillation. The antioxidant used is Vitamin E and the fraction used in NOνA is based on the experience of the MACRO experiment [2].

Filling horizontal cells is more complex than filling the vertical ones. For horizontals, if the cells are angled slightly higher at the far end with respect to the filling end, then the cell is not able to fill completely and thus will not generate light throughout the cell as it was designed. For the NDOS, an air pump was used to evacuate the air pocket and fills the cells to a set level. Later the cells were topped-off with scintillating oil. The Far Detector is planned to have the the horizontals tilted in such a way that this is not necessary. We also discovered leaks in some of the modules. This was later confirmed by a subsequent performance check using cosmic ray muons as described in Section 2.3. Figure 1.17 shows a leak in one of the affected modules.

1.2.3 Wavelength Shifting Fiber

The light generated in the scintillator and reflected inside the PVC module is eventually collected by a double cladded wavelength shifting (WLS) fiber. The fiber is the Y11 Kuraray wavelength shifting fiber manufactured by Kuraray. This fiber is strung along the entire length of the cellular cavity, looped at one end, then strung back along the length to be doubly read out by the APD. The fiber is a blue light to green light WLS with a diameter of 0.7 mm. This size was chosen for the effectiveness of using twice as much fiber with respect to using a single thicker fiber. The looping provides the readout with nearly 4 times as much light yield when compared to a single fiber with a non-reflective end. Additional light is helpful since it enhances the signal from the far end where there are no APDs. The other purpose of going with this

method was to have only one readout side for each orthogonal view. A relative position of the traversing charge particle could be calculated using the time difference of the arrival of light from both ends of the fiber.

1.2.4 APDs and Electronics

The photodetector device used on each of the NOνA detectors is an avalanche photodiode (APD) produced by the Japanese company Hamamatsu. They come as a package of an array of 32 pixels, made of silicon as the detection material, fixed to a carrier board substrate using flip-chip mounting. Figure 1.10 shows a close-up of the APD pixels on the carrier board. The device was custom designed to allow for the two ends of a fiber from one channel in the detector to fit over each pixel. Each of the 32 pixels map directly to the 32 channels in an extrusion module [2]. The reason for choosing the APDs over traditional photomultiplier tubes (PMT) is the higher quantum efficiency when using wavelength shifting fiber out to 15 meters in the Far Detector from the device. At the range of wavelengths of light from the fiber incident on the APD, the quantum efficiency is 85% compared to 10% from the PMTs. The carrier board that the APD is attached to is thermally isolated from the other electronics to minimize thermal load.
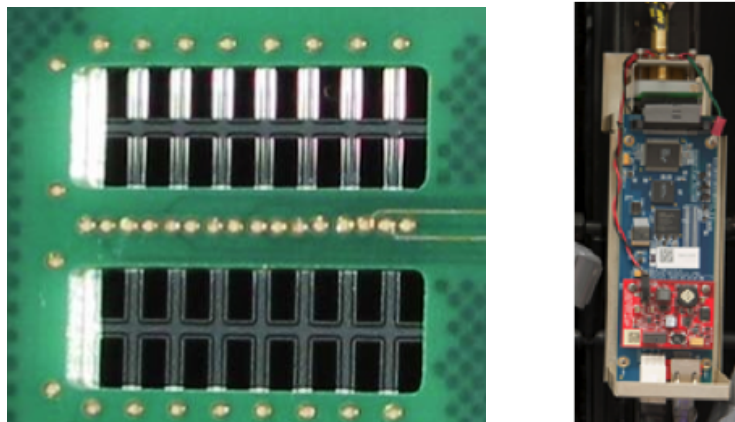
Figure 1.10: A photograph of the 32 silicon APD pixels on its mounting board and another photograph of the FEB with the APD and cooling system attached to the NDOS.

To reduce the noise levels within the APD, thermal cooling of the electronics to -15°C is necessary. This reduces what is called bulk dark current, which can cause considerable noise

in the detector. The coolers are a combination of thermoelectric coolers and a water cooling system. The thermoelectric coolers remove any heat from inside the APD to itself, where it is transferred to a heat sink. In this case, the heat sink is the water cooling system that circulates cool water to each thermoelectric cooler and pumps the warmer water back to start the cycle again. Figure 1.11 shows a schematic of how the cool water is transferred and recycled along the Far Detector to each APD.
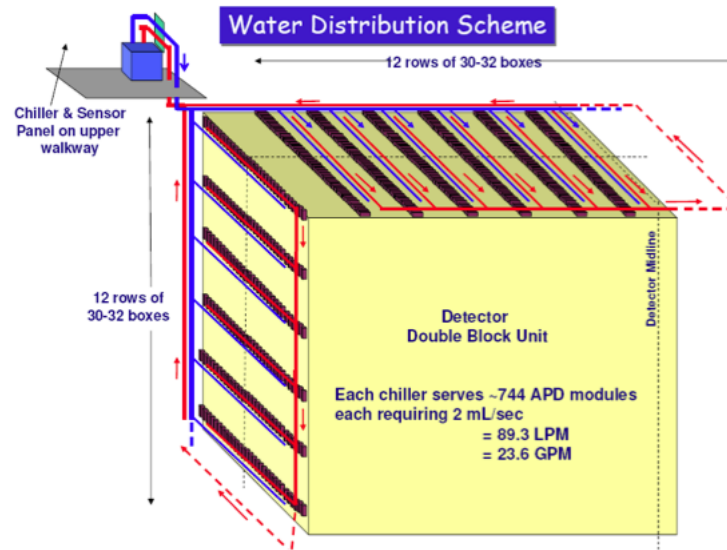
Figure 1.11: A schematic of the cooling system for the Far Detector showing the cycling of cool water as a heat sink for the electronics [2].

The APD mounted on the carrier board within the thermoelectric cooling system is attached by a ribbon cable to a front-end electronics board (FEB). Also in Figure 1.10, the FEB can be seen attached to the NDOS without its protective covering. The FEB not only contains the connector for interfacing with the data acquisition (DAQ) system, but also the thermoelectric cooler controller circuitry, the digital-to-analog converter (DAC) and analog-to-digital converter (ADC) for control and monitoring, and a field programmable gate array (FPGA) [2]. Once the readout is digitized, the data is sent to a data concentrator module (DCM) where data is combined from 64 FEBs and stored for later analysis. Figure 1.12 shows a DCM attached to the NDOS with cabling coming from the FEBs.

Figure 1.12: A photograph of a DCM where up to 64 FEBs synchronize data collected in a spill window to then be stored in a computer for later processing.

Among the goals of the NDOS is to test the deployment of a large number of APDs under realistic conditions. A number of issues were encountered and then solved. As an example it was found that the water in the surrounding air was condensing on the surface of the cooled APDs which could eventually damage them. The solution was found to be removal of the moist air from the space around the APD with an active air drying system. This is essentially a pump that passes pure nitrogen gas over the cooled APD to prevent condensation. Another issue was that liquid scintillator would set on the surface of the APD causing large amounts of noise in pixels after prolonged exposure. Oil can travel up the bundles of fibers and out the manifold (if they were not sealed properly) onto the APDs in a process called wicking. The current solution under testing involves protecting the APDs from contaminants using some form of coating applied to the silicon. Two types of coatings on the surfaces of the APDs are currently being tested. A silicon coating has been applied by Hamamatsu, the manufacturer of the APDs, and a parylene coating has been applied by the US based company Advanced Coating as an alternative protectant.

1.3   NDOS Performance

NDOS serves as a demonstration of not only the construction process, but also that we can obtain the NOνA physics analysis goals. We use the fact that cosmic ray muons are traversing the detector continuously and we can see neutrinos from the NuMI beam. The data collected by

the NDOS is utilized in the development of the simulation, reconstruction, and calibration. The demonstration of the physics goals rely on the performance of the development in those areas. Since this is a prototype detector, issues occured and were solved to prepare for the construction of the Near and Far Detectors. The NDOS within this time experienced reconfiguration of the APDs throughout the detector. During the initial phase of construction, the NDOS was adding more APDs to the detector. When testing of the cooling system occurred, some APDs failed and had to be removed causing loss of detection coverage. Another loss to detection coverage occurs from noisy pixels in the APDs. These channels often show high levels of readout continuously throughout data collection. Channel by channel masking is determined and applied to data to prevent reconstruction algorithms using the noise as apart of track determination. In this section I will discuss the cosmic ray muons, the performance of the NDOS using the cosmic ray muons, and neutrino data.

1.3.1   Cosmic Ray Muons in the NDOS

Understanding the performance capabilities of the NDOS can better prepare us for the construction of the NOνA Near and Far Detectors. A reconstruction for the cosmic ray data has been developed and exercised. As an example, the cosmic ray muon rates have been observed in the detector as well as neutrinos from the beam. Figure 1.13 shows cosmic ray muons traversing the NDOS in a 500 μs spill window. The channel by channel masking is set on the data indicated by the light grey boxes that correspond to inactive channels. The colored dashed lines running through the energy deposition in each channel are the reconstructed cosmic ray muon tracks.

Simulation and reconstruction has been developed for the data, and the performance and expected physics results have been analyzed. For cosmic ray muons the reconstruction has an efficiency greater than 98%. Figure 1.14 shows this efficiency in the Monte Carlo both with and without channel by channel masking.

The rate of cosmic ray muons traversing the detector can be calculated from the expected rate at the Earth surface (i.e. 1 muon/minute/cm^2) and the top surface area of the detector which was approximately 1.17×10^5 cm^2 during the first half of the running period in 2011.
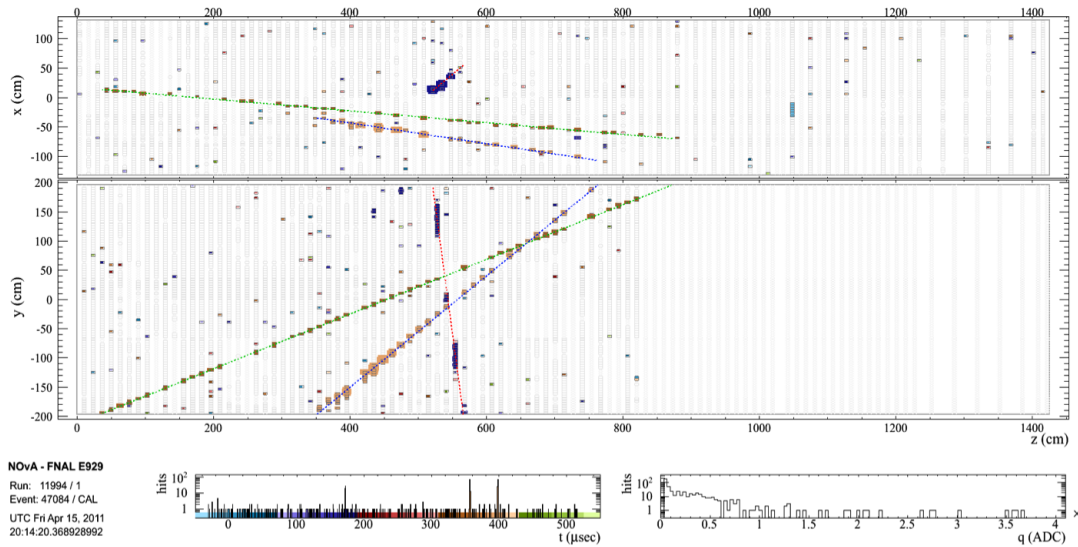
Figure 1.13: This show a two plane 2-D event display of the orthogonal planes in the NDOS. The X-Z plane in the top portion is what the event looks like from the top of the detector, approximately 260 cm across. The Y-Z plane in the bottom portion what the event looks like from the side of the detector, approximately 390 cm in height. The dashed lines running through the energy deposition in each pixel are the reconstructed cosmic ray muon track. The dark grey squares are active channels and the light grey squares are masked. The first distribution on the bottom shows the number of hits recorded as a function of time in the spill. The second shows the number of hits as a function of recorded energy deposition within the cell.

This results in a cosmic ray muon rate estimate of 1.95 kHz [7]. Figure 1.15 shows the measured cosmic ray muon rate as a function of time in the NDOS. This is calculated as the number of tracks per 500 μs data collection window modified by ratio of the average number of active channels in the stable run period (4500 channels) and the total active channels during that subrun (about an hour of data taking). As it can be seen in the figure the rate changes over time as APDs are added in the early months and then removed after October 2011 therefore changing the surface area of the detector. Furthermore a comparison of the cosmic rate as a function of time with the number of active channels can be done by comparing Figure 1.15 and Figure 1.16. There is a clear correlation in the drop of the cosmic rate and that of the APD channels around the October 2011 date.
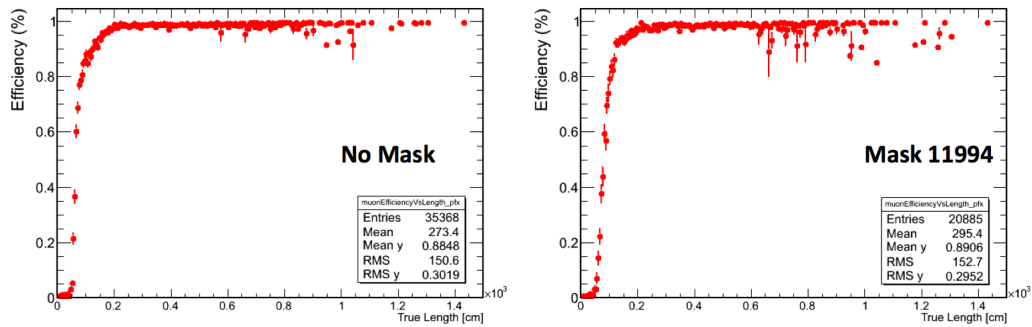
Figure 1.14: These distributions are a side by side comparison of the efficiency of the cosmic reconstruction as a function of track length. This example comparison is simulated cosmic ray muons with and without the channel by channel masking from run 11994 of data taking [8].

Another measure of performance is the mean energy deposition or light level for cosmic ray muons as a function of time as shown in Figure 1.17 (see Section 2.3 for more details of this calculation). This is shown for 8 channels in one module. In the figure it can be seen that the the for one channel (plane 15 cell 30) the light level is low inducing that there are low amounts of scintillator in that cell. Figure 1.17 also shows that same cell was topped off in May 2011 raising it to the mean light level of the others in the same module. However after a while the same cell starts to fall off, followed by other cells also falling off. This behavior was connected to a leak of the scintillator oil. As the leaking occurred, the highest cell in the horizontal plane with light level readout, began to lose light level until it lost all the the oil, then the next
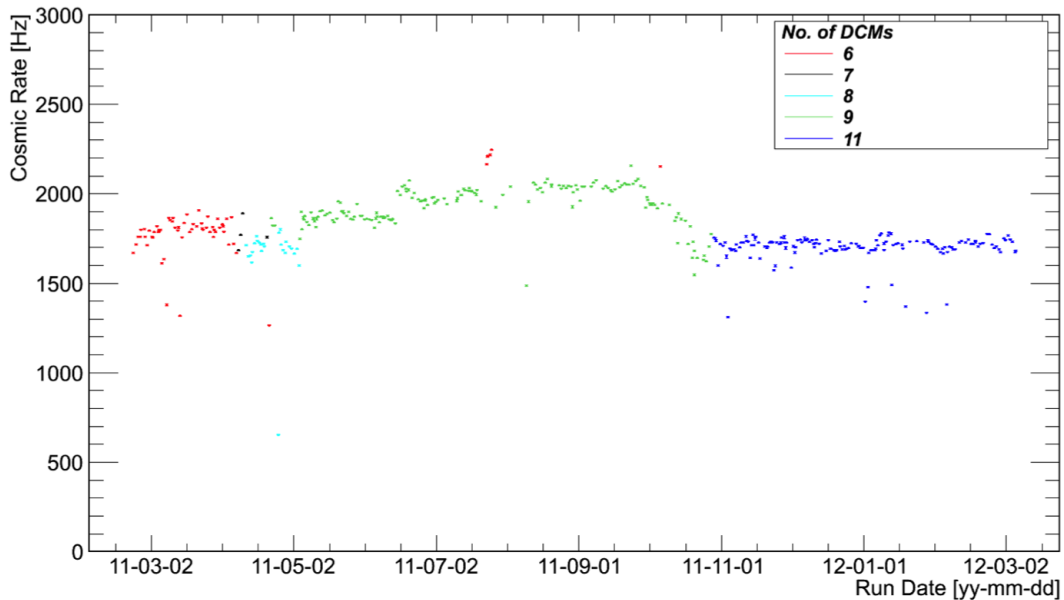
Figure 1.15: This distribution shows the cosmic rate in the NDOS as a function of time. Each color corresponds to the number of active DCMs coming online which is proportional to the number of active channels in the detector [7].

channel lost its oil and light level. Finally, in the figure it can also be seen a change in the light level due to cooling of the channel and subsequent gain level change. This is an example of how we use these data to pinpoint problems that which may occurs in the much larger Far Detector which would have about 360,000 channels.

1.3.2 Neutrinos in the NDOS

Another key physics performance parameter is the observation of neutrinos from the NuMI beam. We expect to see the neutrinos arrive at the detector 222±5 μs after the DAQ system samples the readouts for a total of 500 μs which is called the data trigger. Figure 1.18 shows this spill window with the NuMI beam peaked at 222 μs. This sampling coincides with the NuMI beam hitting a pulse of protons onto a target called the spill, and this spill time is about 10 μs and happens every 2.2 seconds [9]. Figures 1.19 and 1.20 each show a different muon neutrino candidate in the detector. These two event displays show neutrinos in different configurations of the NDOS corresponding to December 2010 and November 2011.
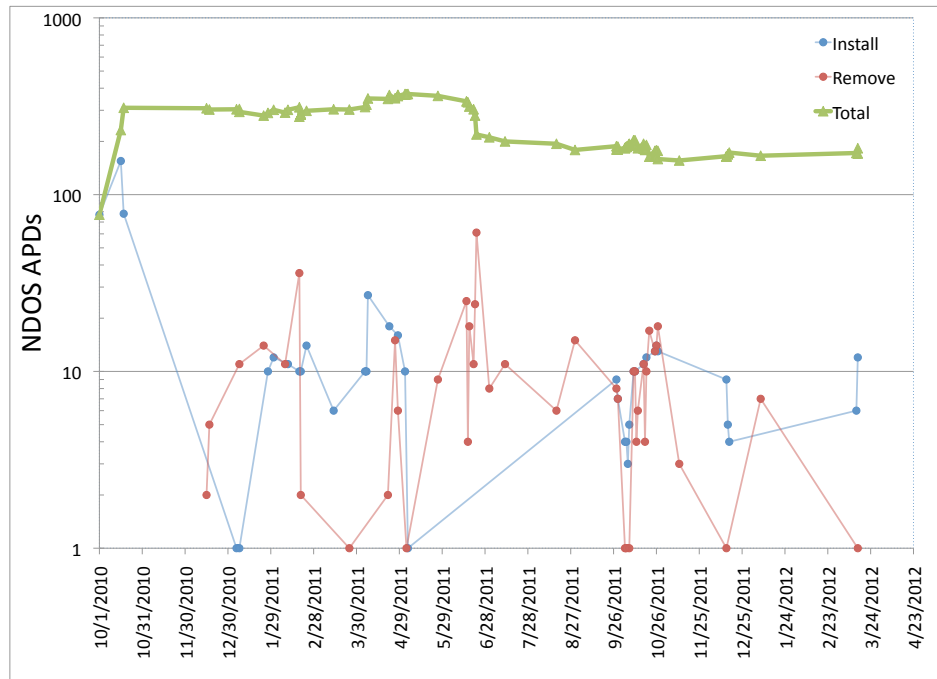
Figure 1.16: This distribution shows the number of active channels in the NDOS over the time it has been collecting data from the NuMI beam. The total number of APDs in the NDOS is the green line. The points in blue and red indicate addition and removal of APDs from the NDOS respectively. Comparing to the cosmic ray in Figure 1.15 we can see the rate fluctuating over time in the same manner as the number of APDs [7].
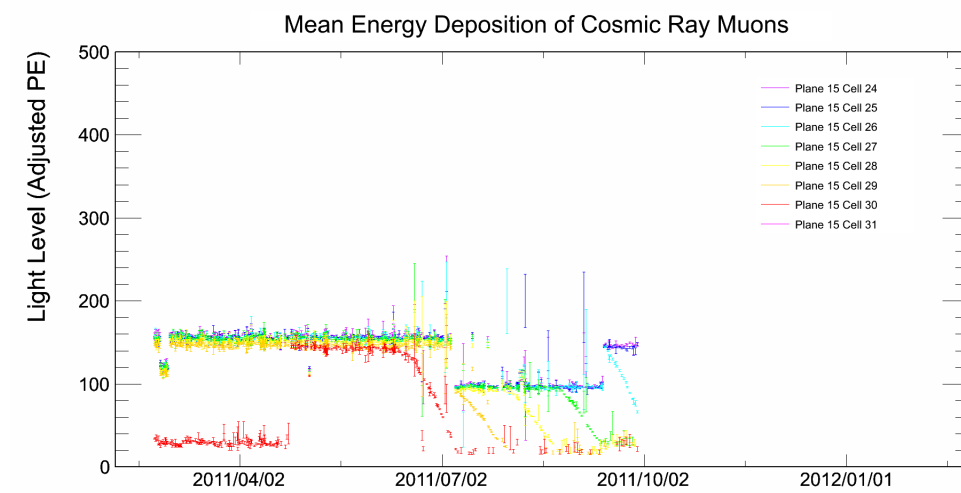
Figure 1.17: This distribution shows the light level in 8 channels on an APD as a function of time. Each color corresponds to one of those 8 channel responses. The first low point is due to low levels of scintillator in the that cell, once it was filled the light level returned to a value similar to the other channels. The slow cascading drop of light levels in these 8 channels is due to a leak in the module. The general shift in light levels in July through September are due to cooling tests on the APDs.
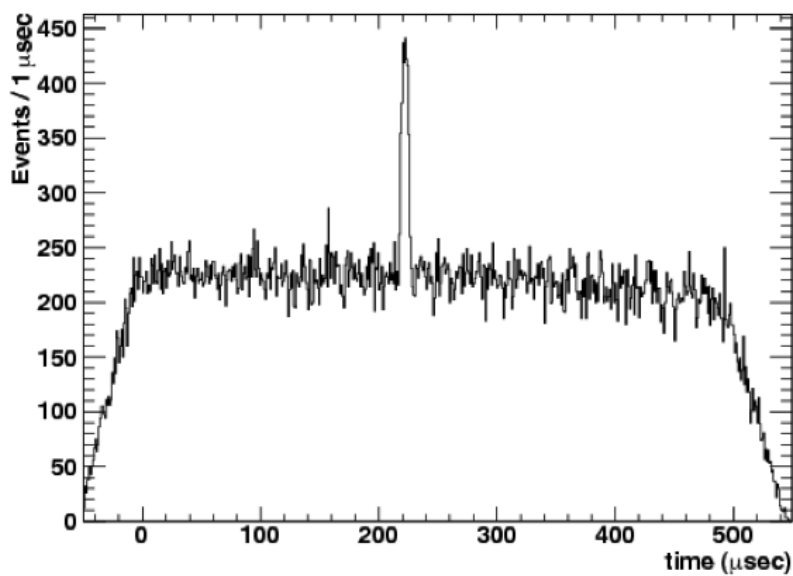
Figure 1.18: This distribution shows all tracks produced within the NDOS during the data trigger corresponding to the NuMI spill time. Cosmic ray muons were cut from the sample as an obvious background. It is clearly seen that an excess amount of tracks are produced within the NDOS at about 222 μs, indicating that the detector is synchronized with the NuMI beam spill. For this distribution, one event means one reconstructed track within the spill window. The ramp-up and fall-off is due to a 50 μs variation on the start of a spill window.
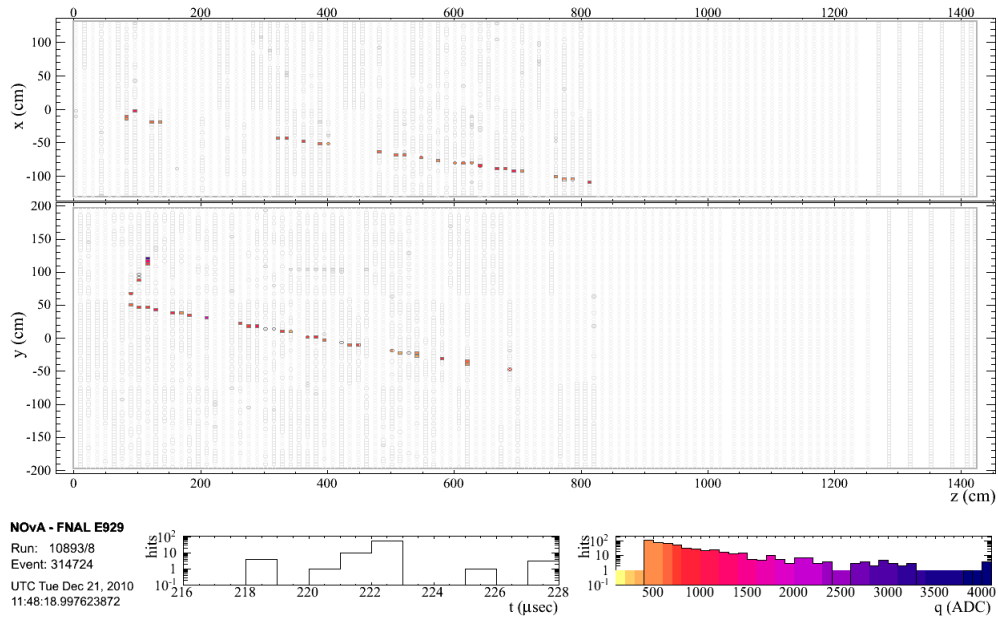
Figure 1.19: This shows a muon neutrino candidate in the NDOS prior to cooling and subsequent reconfiguration of the APDs. The color indicates the amount of energy deposited in the channel from each charged particle. The first bottom distribution is the number of hits within the 10 μs trigger time window. The second distribution shows the number of hits as a function of recorded energy deposition within the detector. The color indicates the range of energy deposition.
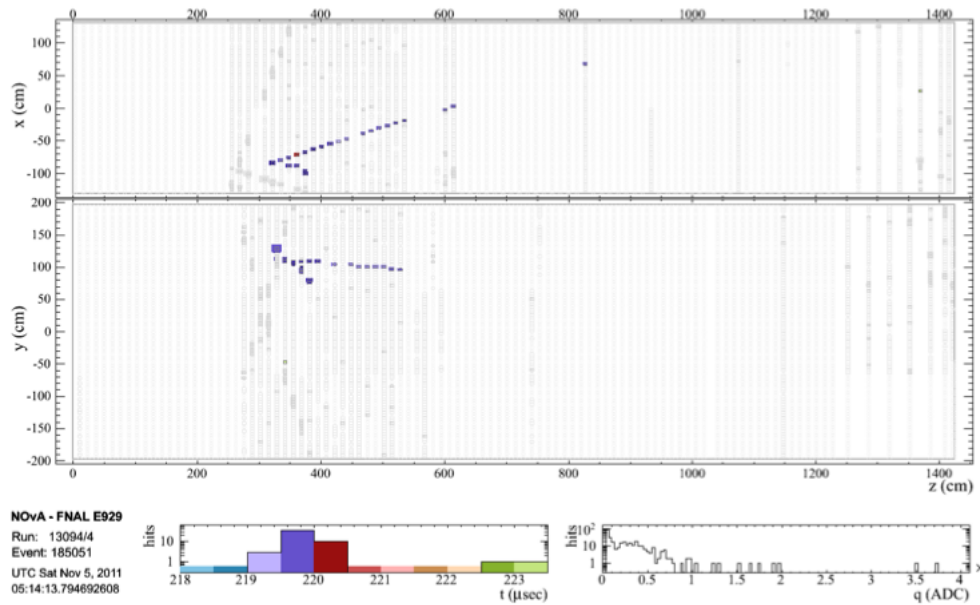
Figure 1.20: This shows a muon neutrino candidate in the NDOS after the cooling and reconfiguration of the APDs. The color indicates the time of the energy deposition in the detector. The size of the squares in the event display indicate the relative amount of energy deposition within each channel. The first bottom distribution is the number of hits within the 10 μs trigger time window. The color indicates when the hit occurred in time. The second distribution shows the number of hits as a function of recorded energy deposition within the detector.

CHAPTER 2. NDOS Detector Calibration

Any physical quantities to be measured experimentally require calibration of the experimental apparatus. In the case of particle physics, the calibration of the detectors involves removing the variations within each detector, relating the energy deposition between different detectors, and translating the detector response for different types of particle to understood energy units such as GeV. We have used the NDOS in NOνA to develop the calibration techniques that will be eventually applied to the Near and Far Detectors. In this thesis I will focus on describing the calibration related to detector response within the NDOS and its time evolution.

The following sections I will explain that we use cosmic ray muons to carry out these calibrations. I will also highlight the corrections obtained to obtain a uniform detector response over all the cells in the detector as well as throughout the entire data taking period.

2.1   Using Cosmic Ray Muons for Calibration

For detector response calibrations of the NDOS, we use cosmic ray muons. These particles are abundantly produced and continuously traverse all parts of the detector. Figure 1.15 shows the rate of muons traversing the detector every second as a function of time. Another reason to use the cosmic ray muons as a calibration source is that they are completely independent from the physics data sample that is going to be analyzed. Furthermore this is a useful source of particles to calibrate the detector because muons are minimum ionizing particles. Minimum ionization is the process by which charged particles traversing through a detector interact minimally with that detector and deposit energy uniformly per unit length along their trajectories. Other particles can be used, such as hadrons from a test beam, however these particles can experience internuclear interactions that would not be desirable in calibration. Muons can also

radiate and deposit energy undesirably within the detector by means of bremsstrahlung (the process of a charged particle radiating a high energy photon knocking atomic electrons out of its orbit). This can cause a higher amount of energy to be deposited in the detector.

Quality cuts are used so that assumptions made are not inaccurate and inefficiencies are low and do not cause problems in the calibration. One of the quality cuts on the data used for this calibration is using only cosmic ray muons that traverse the entire volume of the detector. These muons are called *through-going* muons in contrast to *stopping* muons, which are those that stop within the detector volume. Through-going cosmic ray muons are ideal because they are minimum ionizing particles, depositing nearly constant energy along their path through the entire detector. Another cut made on muons used in the calibration is selecting only muons that have a calculated path length of less than 10 cm. Because the cosmic track reconstruction efficiency is lower at steep angles with respect to the surface of the earth, we require the track to pass more planes of the detector for better reconstruction. This gives better precision to the track angle and hence the calculation of the path length. The path length calculation is further detailed below in Section 2.2. Each of the detector response calibrations addresses the various differences each channel has in space and time. These differences come from combinations of different factors within each channel, which I will describe in further detail in each calibration section.

2.2 Spatial Detector Response Calibration

The goal of the spatial detector response calibration is to make the detector response uniform throughout the detector. Two different corrections must be applied to the collected data. One is that the channel to channel response must be the same for a particle depositing the same energy at the same distance from the readout. The second is that the channel response must be the same for the same energy deposition from a particle as a function of distance to the readout. Any corrections to make these variations uniform must take both of these aspects into account. The observed issues that need to addressed in the spatial calibration are the various differences in each of the components that make up the channel. These differences can accumulate to a noticeable variation of recorded energy deposits across channels. These variations come from

several sources such as:

- Scintillator may have slightly more pseudocumene than another batch

- PVC may have less titanium oxide ($Ti0_2$) for reflectivity than other extrusions

- Electronics can also vary due to different handling in installation

- Manufacturing of the APDs will have some uncertainties associated from quality analysis from the manufacturer

This is not an exhaustive list of variation in channels, but it should give an idea of how small variations can combine into noticeable variations in recorded energy deposition for channels. We correct these issues by first finding the mean energy deposition per unit length of the cosmic ray muons, which should be constant throughout the detector. Next we set the amount of light collected in our data, which is proportional to the energy deposition per unit length, to that value as a function of space. This gives us a correction value for each channel and ensures that data collected from each channel will be recorded uniformly across the detector. To do these correction with precision, a large data sample over all time is necessary, so the entire cosmic ray muon data sample is employed.

There are several assumptions made in this step of the calibration: the channel response is stable over time, the energy spectrum of cosmic ray muons is uniform as a function of detector depth, and that the detector response to arriving photons is linear. The assumption about the energy spectrum of the muons is reasonable for the NDOS, though this will eventually need to be reexamined in the Far Detector. The Far Detector provides shielding from the cosmic rays in the lower parts of the detector because its dimensions and mass are much larger than the NDOS. This can be mitigated, but not entirely eliminated, from the fact that cosmic ray muons deposit energy approximately uniform across a wide range of energies [10].

Attenuation is the process of losing photons in the material of where they propagate, usually by the dispersive properties of the material itself. The detector uses long channels to collect light into fibers from charged particles. Photons in the detector must travel over the distance of the cell through the fibers. This is especially important in the Far Detector. In Figure 2.1, we

can see from the energy deposition distributions that different amounts of light are collected in certain ranges of the channel length. The units of ADC represent the signal response, or number of photoelectrons, we record from the APD light collector. The W value is the reconstructed position a charged particle deposited energy along the length of a channel. The positive ranges are positions along the channel that are close to the APD and ranges that are negative are further away from the APD. Looking at the black distribution, we notice the peak of the distribution is lower and the tail is smaller than the rest indicating more light loss will occur the further light is generated in this channel from the APD. The gold distribution has a higher value and a larger tail indicating the light generated in this region does not travel as far and will experience less attenuation. We can also see that the recorded amount of light decreases the further away the charged particle was from the APD. To be able to obtain a uniform detector response, we must first correct the amount of light collected from a cosmic muon passing through at different distances from the readout to the same light level. This is not a large effect in the NDOS and Near Detector but will be important in the Far Detector.

We need to apply attenuation fits on a channel by channel basis, but we need to first correct by the path length of the muon depositing energy. This is to avoid being sensitive to differences in the path length distribution of the muons. Some of these differences in path length can arise from reconstruction inefficiencies of different track angles in the presence of masked channels or detector self-shielding. During the process of calculating the correction to attenuation, the path length of the cosmic ray muon in a channel is calculated. We calculate path length of the cosmic ray muon in order to determine the energy deposited per unit length. The path length calculation for a cosmic ray muon is done through an estimation process. It works by first qualifying a channel with respect to other channels, active or not, around it. The process then uses the track angle and physical dimensions of the cell to calculate the path length within that channel. For example, Figure 2.2 shows a track going through three active channels in the same module and depositing energy in each. The process selects the dark red channel in the center and asks if the channel above and below it have energy deposition. If so, the path length can be easily calculated. If not, the path length will be calculated in another formula to find the most likely path length the muon traversed in the cell.
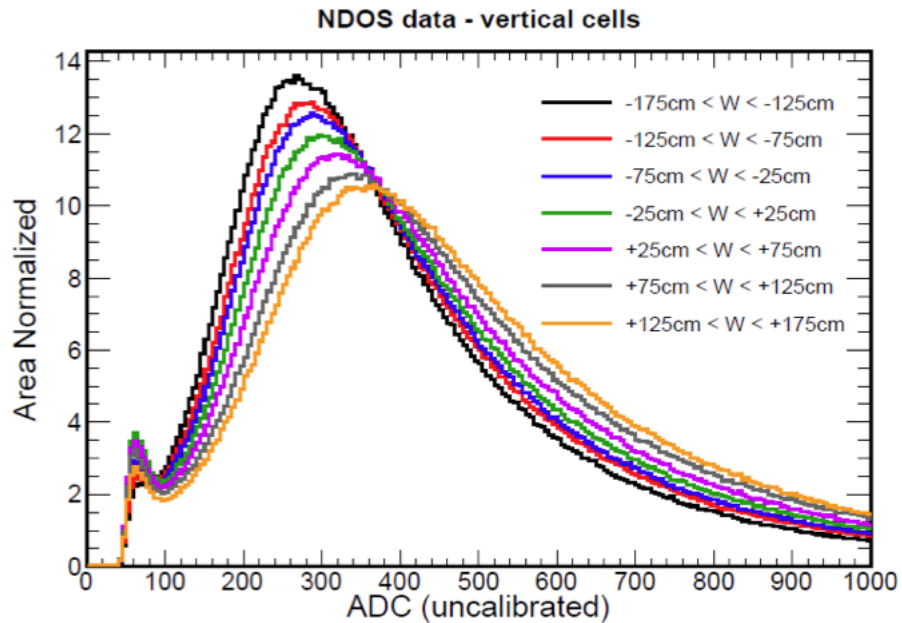
Figure 2.1: These distributions shows the number of hits as a function of energy deposition (ADC) of cosmic ray muons in all vertical channels from all cosmic ray muon data collected. The different colors represent the various position ranges along the length of the cell. The green is the central region of the channel between -25 and 25 cm, where 0 represents the center of the channel. Positive W positions are represented by the gold, grey, and violet distribution and have peaks at the highest energy deposition value due to the fact this side is nearest to the photodetector. The negative W positions are represented by the black, red, and blue distributions and have peaks at the lowest energy deposition value due to the fact this side farthest from the photodetector. [10].
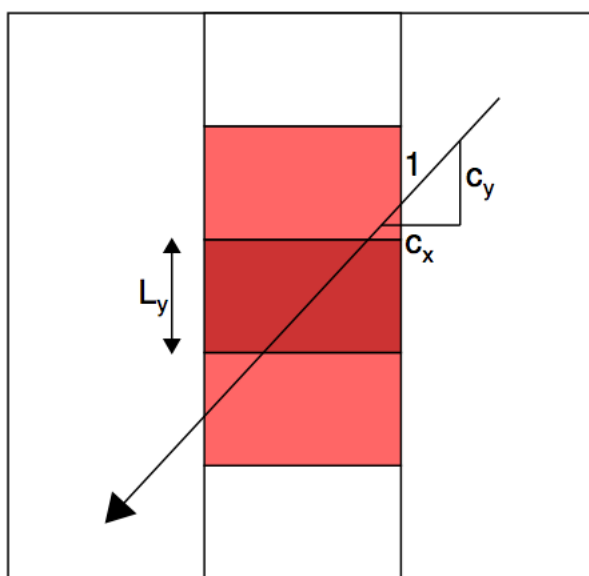
Figure 2.2: This is an example of the qualification of a channel to determine the path length of the muon traveling through it and depositing energy along the way. Since there are energy deposits from the muon track above and below the dark red channel, the path length in the cell is calculated as L_y/c_y. L_y is the height of a channel and c_y is the unit height or the sine of the angle with respect to the surface of earth the muon track makes. [10].

To calibrate the light being collected, a functional form of the energy deposited per unit length for certain position along the channel is found. In Figure 2.3, an example channel with energy deposited per unit length for several positions along the channel are plotted. A functional form is found by a fit which has two key features. The attenuation of the cell is described by the exponential rise in the distribution. The form is given as:

$$y = C + A \left(exp \left(\frac{x}{X} \right) + exp \left(-\frac{3L/2 + x}{X} \right) \right) \tag{2.1}$$

Where y is the response , x is the position along the channel, X is the attenuation length, and L is the length of a channel. The 'roll-offs are the features at the near and far ends of the channels. This was empirically found to be x^4 function. The fits are done on channel by channel basis using all data collected over the run period. An attenuation function is obtained for each channel in the detector. We can then calculate a correction factor by finding the position along a cell where a changed particle deposited energy and inserting that value into the function. Each channel has its own function based on fits of the data collected over all time. We calculate the correction factor by finding the position along the cell where a charge particle deposited energy and inserting that value in the function. This will bring the amount of light collected by the APDs to a value that the APD should see, which translates to the amount of energy deposited by the particle in the channel.

Once we obtain an attenuation correction for each particle, we must then normalize the energy deposition of all channels to a common point. We correct this by setting the mean energy deposition of each channel to the same mean energy deposition per unit length. To do this, we find the mean energy deposition per unit length from all data in all channels. This value is now the expected value of a minimum ionizing particle's energy deposition per unit length throughout the detector. This completes the spatial corrections of the detector and gives us an unit of energy deposition in the detector called PECorr, or spatial response corrected PE. This is a correction that is done using the entire data taking period, and will not correct for the variations over time.

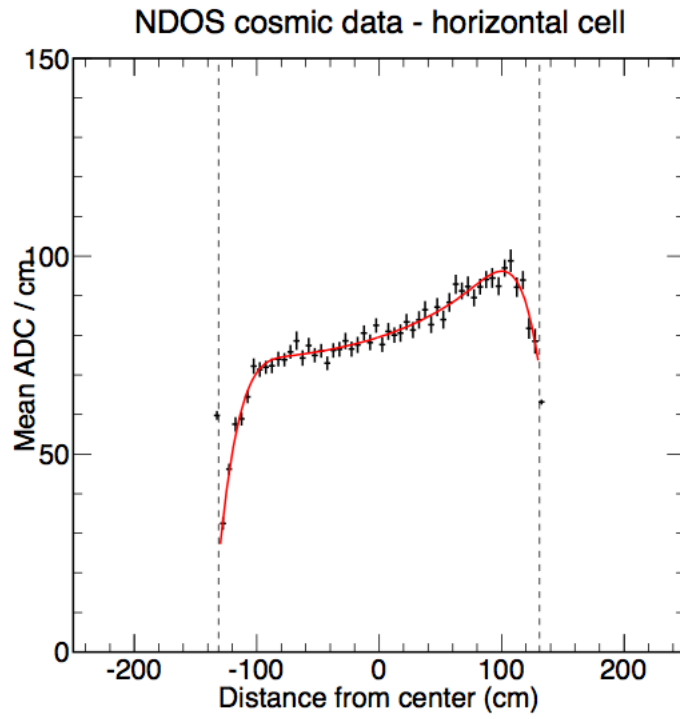Figure 2.3: This shows the mean energy deposited as a function of distance along the channel from the readout. This uses all the cosmic ray muon data to create this distribution. The readout is located at the positive end of the distribution at the dashed line. The other dashed line represents the far end of the channel where the fiber is looped. The fit of the data is applied indicated by the red curve [10].

2.3   Temporal Detector Response Calibration

The temporal energy calibration is a correction for the variation of energy deposited in the detector over time. The spatial energy calibration instead ensures that, energy deposition in recorded data is uniform in space but not that it is uniform over time. I will detail in this section the data quality and applied cuts on data, the selection of the mean energy deposition, and finally the time drift point calibration.

2.3.1   Calibration Data Selection

In order to carry out this aspect of the calibration we select reconstructed cosmic ray muon tracks in the detector. In Figure 1.13, we can see the event display of cosmic ray muon tracks depositing energy in the detector. For reconstruction the tracks are assumed to be straight line tracks, with no bending due to scattering in the detector. Tracks at steep angles are not likely to be well reconstructed. In addition, inactive channels in the detector reduces the track reconstruction efficiency. In order to ensure that we use only quality reconstructed tracks, we use only tracks that transverse at least eight planes for the detector. The efficiency of reconstruction as a function of number of planes that the track transversed is shown in Figure 1.14. In this figure it can be seen that the 8 plane (approximately 0.5 m in length minimally) selection returns a reconstruction efficiency of 50% or better. Reconstructed tracks that follow this condition allow for a better path length corrections which is useful for more precise energy deposition calculations.

I also studied the possibility of an additional selection requiring the track to traverse continuous planes in the detector. This would ensure that the track would cross both $\hat{x}$ and $\hat{y}$ oriented planes for better three dimensional reconstruction. However, this cut was problematic in the NDOS since many channels were inactive during commissioning and thus it has not been used here.

A sample of cosmic ray muons with the 8 plane quality cut can still present catastrophic energy loss effects such as bremsstrahlung. In order to deal with this, the total energy deposition distribution is truncated to remove the highest 5% of energetic depositions [11] as can be seen

in Figure 2.6b (more detail in Section 2.3.2).

Ideally stopping muons should be removed from the sample, since these muons create higher energy deposition in channels than when the muon is minimum ionizing. Stopping muons are considered to be any muon that has an end of the reconstructed track within the *stopping muon volume*. For this analysis the stopping muon volume is considered to be ± 110 cm from the center of the detector along the width ($\hat{x}$-direction), -160 cm and +197 cm from the center of the detector along the height ($\hat{y}$-direction), and between 240 cm to 1200 cm from the beginning of the detector (along $\hat{z}$-direction). The ratio of stopping muons to total muons from reconstructed tracks is 10.1%, as it is shown in the bottom right of Figure 2.4. Stopping muons would need to be removed from the sample, but in this analysis have not been removed. Figure 2.4 shows distributions of the end points of reconstructed tracks in the detector. The lines in the figure highlight the volume described above. The distribution of these end points, i.e. within the stopping muon volume, is roughly uniform. These muon tracks are spatially distributed uniformly within the volume and will deposit the same energy homogeneously throughout the detector in each channel. Thus all channels are getting same extra energy deposition from decaying muons, and the energy distributions will not be different from channel to channel [12]. This will not be the case in the Far Detector as the number of stopping muons will vary as a function of depth.

2.3.2   Mean Energy Deposition

Minimum ionizing cosmic ray muons (MIP-like) can be used as the standard candle to correct any changes in gains that occur over time. Once cosmic ray muons have been selected to be well reconstructed and with a homogeneous distribution over all cells in the detector, we can study the energy deposition distribution for each cell or group of cells and obtain the mean energy deposition as the point to compare among cells and across time. In order to accumulate sufficient statistics of muons crossing one cell we must use one day of data taking of cosmic muon data in the NDOS which is the definition of a run.

In figure 2.5a, I show a distribution of the energy deposited from all channels combined from the NDOS for a single run. This distribution is not symmetric, in fact it has the form of a
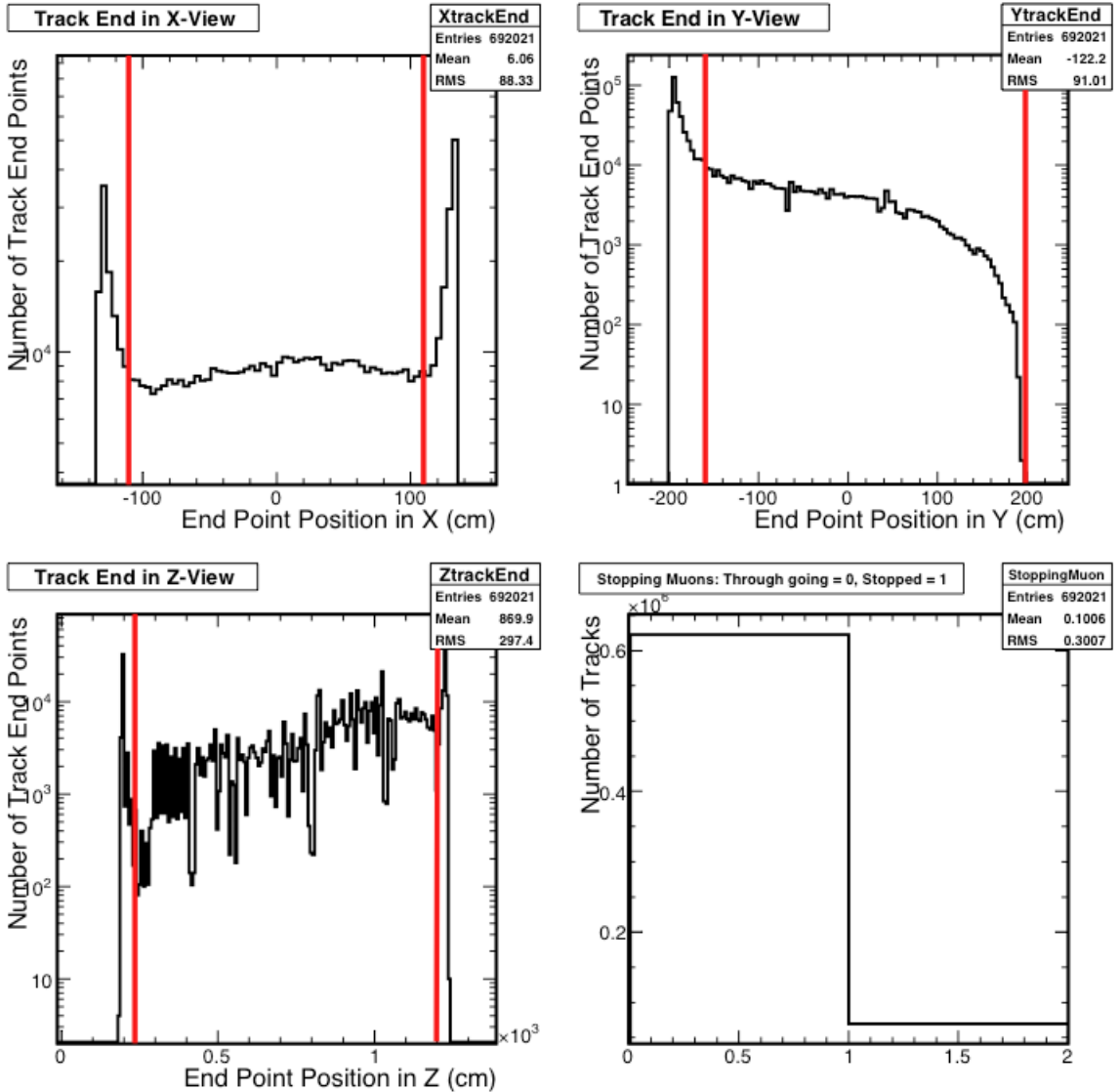
Figure 2.4: *Top Left:* The distribution of end points of tracks in the $\hat{x}$-direction. The large peaks indicate where the track has exited through the sides of the detector. *Top Right:* The distribution of end points of tracks in the $\hat{y}$-direction. The large peak at about -197 cm indicate many tracks seen in the $\hat{y}$-direction exit through the bottom of the detector. *Bottom Left:* The distribution of end points of tracks along the $\hat{z}$-direction. The large peaks seen at about 200cm and 1200cm indicate that many of the tracks are leaving the detector regions with active APDs. *Bottom Right:* The number of number of through going muons versus the number of stopping muons. Track ends inside the stopping muon volume defined by (x_{min}, x_{max}; y_{min}, y_{max}; z_{min}, z_{max}) = (-110 cm, 110 cm; -160 cm, 197 cm; 240 cm, 1200 cm) are considered stopped muon, and everything else is considered a through-going muon. The percent of stopping muons to total number of through-going muons is 10.1%. The red lines indicate the stopping muon volume within the NDOS.

Landau distribution which describes the energy deposition of charged particles traversing a thin strip of material. The distribution shown in the figure is actually a convolved Landau-Gauss distribution, where the Gaussian form describes the energy resolution within our detector. The choice of the mean energy deposition comes from choosing the most probable value (MPV) or the arithmetic mean, or simply the mean, of the distribution. The MPV of the distribution is the value with the highest frequency from randomly sampling the recorded energy depositions in a channel, basically the peak of the distribution. The mean of the distribution is the sum of all energy depositions divided by the number of depositions. Since this distribution is not symmetric, the mean and the MPV are distinct, as seen in Figure 2.6a.

Ideally, I would like to obtain and use the MPV as the representative mean deposition for the run in each channel. In Figure 2.5a, the fit applied to the distribution looks reasonably good, even though the fit runs somewhat higher in the peak and somewhat low near 200 PECorr[†], the rise and fall after the peak and the tail fit well. Using these fits, we find the MPV. Unfortunately, obtaining the MPV requires fitting this convolved Landau-Gauss function to the data which is computationally time consuming. This would be even more expensive in the Far Detector calibration, which has about 23 times as many FEBs as the NDOS.

An alternative to using the MPV is using the mean of the distribution. However, as it is shown in Figure 2.6a, the mean is quite far from the MPV. In the MINOS experiment [13], the mean energy channel to channel calibration was done by using the truncated energy deposition distribution in order to move the mean to the MPV. The remainder of Figure 2.6 shows the process of truncating the distribution from 5% to 25% of the most energetic deposition in the channels in 5% intervals. As it can be seen, we would need to truncate more than 25% of the distribution to get better than a 40% difference of the MPV. Thus we have determined that truncation is not helpful to obtain a value closer to the MPV. We do, nevertheless, use the truncation of 5% as shown in Figure 2.6b in order to eliminate high energy depositions such as those arising from bremsstrahlung and noisy channels.

[†]spatial detector response corrected PE
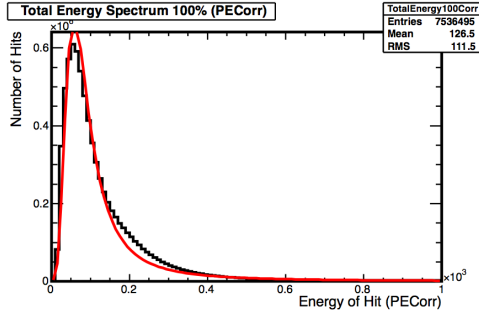
(a) No energy deposition removed from distribution.
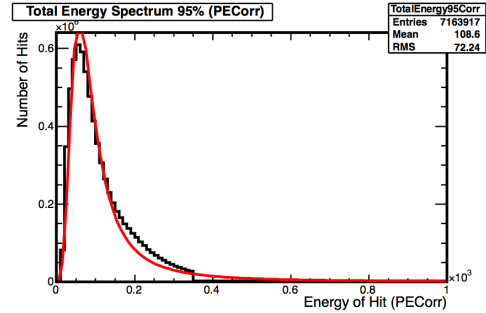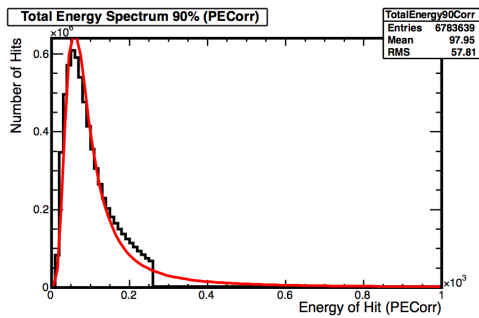
(b) 5% most energetic depositions removed.

(c) 10% most energetic depositions removed.
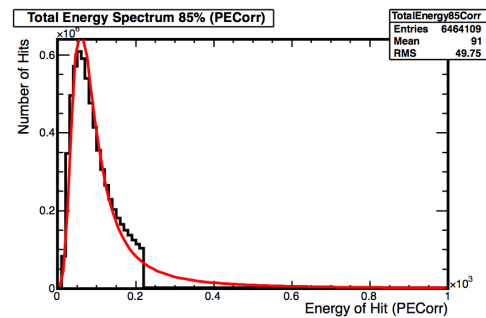
(d) 15% most energetic depositions removed.
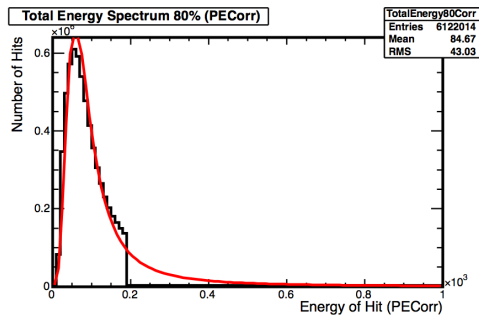
(e) 20% most energetic depositions removed.
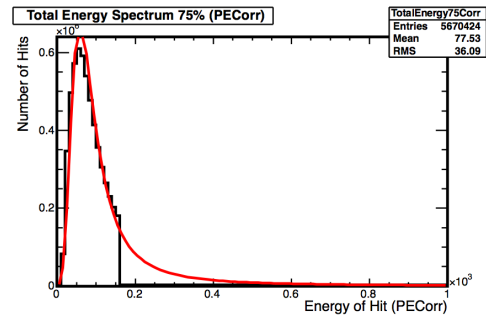
(f) 25% most energetic depositions removed.

Figure 2.5: The total energy deposition distribution for all active FEBs in the NDOS fitted to a convolved Landau-Gauss distribution in order to improve the statistics to show the concept of truncating the distribution. This is a comparison of the fit to the total energy deposition distribution with varying levels of truncation on the distribution to match the mean with the MPV.
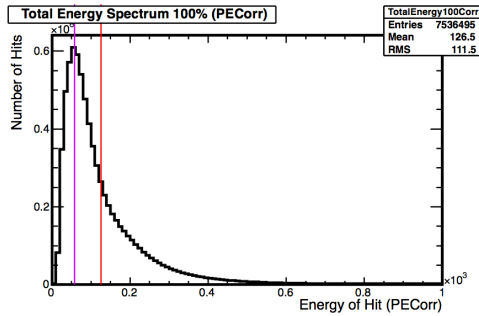
(a) No energy deposition removed from distribution.
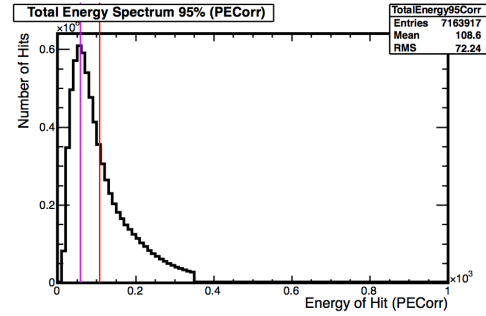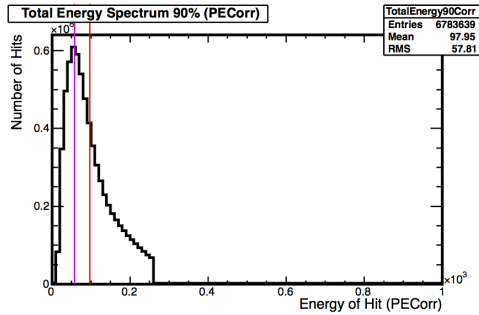
(b) 5% most energetic depositions removed.

(c) 10% most energetic depositions removed.
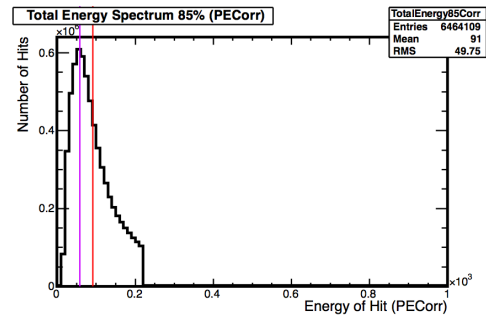
(d) 15% most energetic depositions removed.
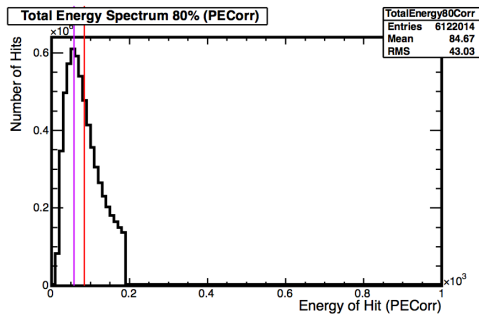
(e) 20% most energetic depositions removed.
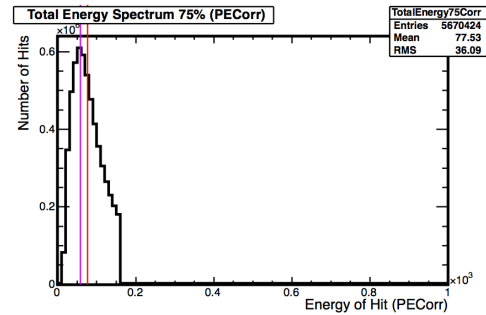
(f) 25% most energetic depositions removed.

Figure 2.6: This is a comparison of the mean and MPV of the distribution with varying levels of truncation on the distribution to match the mean with the MPV. The red line indicates the mean of the distribution shown in the statistics box where the violet line indicates the most probable value (MPV) of the distribution which is 52.4 corrected photoelectrons (PECorr) for this particular run. The fit to retrieve the MPV was a convolved Landau-Gauss fit. The one we use in the temporal response calibration has a 5% most energetic depositions removed, Figure 2.6b.

2.3.3   Drift Point Calibration

The drift point calibration is the process of taking each channel or combination of channels (as in 32 channels of an FEB) in the detector and correcting the light output of each channel to the same level over time. We want to ensure that no matter when data was collected, a cosmic ray muon will be read out as having an equivalent amount of energy deposition per unit length throughout time. This is an important piece of the calibration process as the Near and Far Detectors are planned to operate over a 6 year period and as the NDOS had several significant adjustments to the gains during the data taking period.

The drift point calibration proceeds by obtaining the mean energy deposition per channel. Due to low statistics for some channels and dramatic fluctuations in other channels, the channels have to be combined into groupings of 32 channels corresponding to FEBs. Figure 2.7 shows the 32 individual channels' mean energy deposition as a function of time. Each point represents approximately one day of data taking for cosmic ray muons which corresponds to a run. The error on each point, σ_{mean}, is given by:

$$\sigma_{mean} = \frac{RMS}{\sqrt{N}} \tag{2.2}$$

Where the RMS is the root-mean squared of the total energy deposition distribution for one FEB, and N is the number of energy deposition measurements in that distribution. In Figure 2.7 there are clearly points of low statistics and dramatic fluctuations on a channel by channel basis. Combining the channels helps eliminate many of these issues. We can also see that each individual channel, which corresponds to a pixel on the APD, responds similarly throughout time. This feature can allow us to group all 32 channels into a single FEB, correct the FEB as a whole, and later correct each channel individually.

Figure 2.8 shows all channels grouped into a single FEB for the mean energy deposition distribution. This shows some interesting features. We first notice five distinct time periods that have relatively stable mean energy deposition over time, even though the mean energy deposition shifts abruptly. These abrupt changes correspond to physical or data acquisition (DAQ) related changes. We must correct for the difference in mean energy deposition for each of these periods. The first two periods are periods in time where we were testing threshold
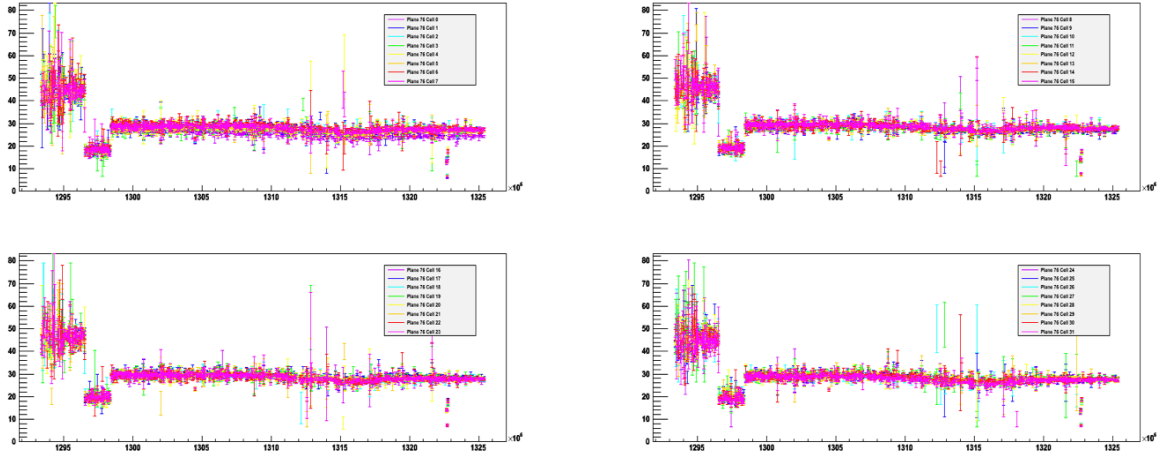
Figure 2.7: The distribution of mean energy deposition of cosmic ray muons over time in the 32 individual channels of one APD. The time is in seconds and started at midnight of 1 January 1970 as a convention of recording the time of an interaction within the detectors. Each color represents one pixel (channel) on the APD.

levels on APD response and high voltage settings. These I refer to as *unstable data periods* due to the erratic settings of the APDs and data collection. The third period I refer to as the *first stable period* of data collection, as the final settings were in place and most of the APDs were installed on NDOS. The fourth region I refer to as the *cooling period*, since some APDs (FEBs) were cooled during this period in order to test the cooling system. Many FEBs do not have this feature, because they were not cooled and remained mostly at a stable mean energy deposition throughout this period into the fifth period. The fifth period is what I refer to as the *second stable period*. The detector was reconfigured because of some APD failures and many of the previous stable period settings were restored.

The next step is to perform multiple χ^2 straight line fits over each FEB. This fit uses a running average to compute the range of the fits and removes *bad runs* from fitting sample. These bad runs are data points that deviate from the running average by 10% or more. These runs are removed because they can skew the fitting line and produce an improper fit and hence an improper correction factor. Natural breaking points were used in the fitting process in order to prevent distinct configuration periods of the detector from being calibrated as one period. An example of this is the visible break point between the second and third periods in Figure 2.8.

The second period in some FEBs has the tendency of becoming indistinguishable from the third period in the fitting algorithm. Figure 2.9 shows the fit lines on the data points for expected time ranges. Once the fitting parameters (i.e. slope and intercept of the straight line fit) have been found, they can then be used to correct each channel in that FEB within a specified time period. Figure 2.10 shows a corrected mean energy deposition over the entire data collection period. The constant for each data point is calculated as follows:

$$d = \frac{k}{AdjPE_{fit}(T)} \tag{2.3}$$

$$DAdjPE_{data} = d \times AdjPE_{data} \tag{2.4}$$

where d is the calibration constant, k is a normalization factor equal to 160.5 AdjPEs, $AdjPE_{fit}(T)$ is the adjusted PE level at the fit line at a given time (T), $AdjPE_{data}$ is the adjusted PE level for the data point, and $DAdjPE_{data}$ is the adjusted PE level with the drift correction applied. Figures 2.11, 2.12, and 2.13 shows the progression of calibration on each FEB for a given run within the APD cooling period. Figure 2.11 shows the uncorrected PE levels in each FEB, then Figure 2.12 shows the FEBs are corrected by the spatial calibration, and finally Figure 2.13 shows the FEBs are corrected by the temporal calibration.

For the calculated correction factors, the data sample used started from run 11570 (February 2011) to run 14022 (June 2012). To gauge the performance of the fits, I use the residual of the data points to the fit line. The equation of the residual is given here,

$$R = \frac{AdjPE_{data} - AdjPE_{fit}}{AdjPE_{fit}} \tag{2.5}$$

where R is the residual, and $AdjPE_{data}$ and $AdjPE_{fit}$ are the adjusted PE levels for the data points and the fit line, respectively. If a data point exceeds a $\pm 5\%$ difference, then the data point should be removed from the sample. If it is a reoccurring outlier in other FEBs, then an examination of why that particular run failed is necessary.

Figure 2.14 shows the residual of the fit line with the mean energy deposition for a run and how well the fits performed in the distribution below the residual. The dashed lines show a $\pm 5\%$ difference of the data point with the fit line. This fitting was done for 363 FEBs in the

NDOS out of a total of 497 FEBs. The total number of runs used in the fitting was 956 runs. The performance of all the fits are shown in Table 2.1. This shows that 98.8% of all mean energy deposition for a run, that had a fit, were within a $\pm 5\%$ difference of the fit line used. The performance of the fits are improved to 99.7% success, when requiring a $\pm 10\%$ difference from the fit line.

	MED for a run	% MED for a run
All data	347028	
All non-zero data	181474	100%
Fitted data points	178009	98.1%
Fitted data points ($> \pm 5\%$)	2118	1.2%
Fitted data points ($> \pm 10\%$)	512	0.3%

Table 2.1: The performance of all mean energy deposition (MED) for a run with respect to their fit lines.
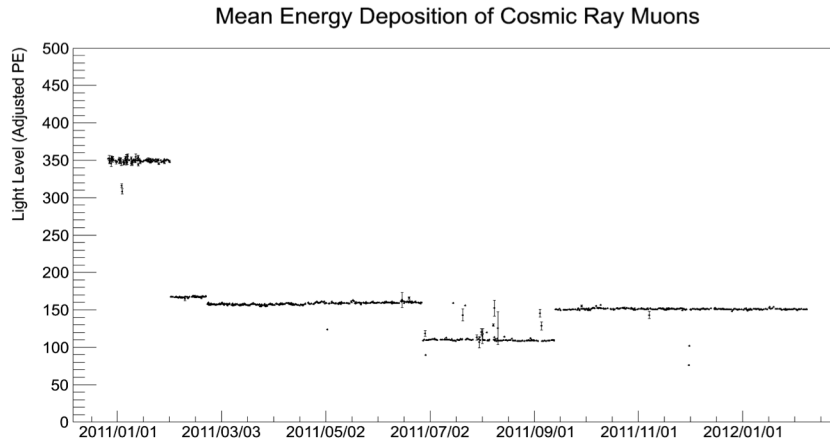
Figure 2.8: An FEB within NDOS showing the mean energy deposition (light level) over time. This combination has reduced dramatic fluctuations and increased statistics for each point. The features of this distribution are the five distinct periods of different recorded mean energy deposition. The first and second period are during the early commissioning of the NDOS and testing the thresholds and voltages on the APDs. The third period is when the thresholds and voltages were kept stable and continuous data collection occurred. The fourth period is when the voltages changed due to cooling of the APD for testing purposes. The voltage was underestimated and the low recorded light level or energy deposition is seen here. Once the testing of the cooling stopped, the voltages were returned to the third period levels and remained in continuous data collection mode.
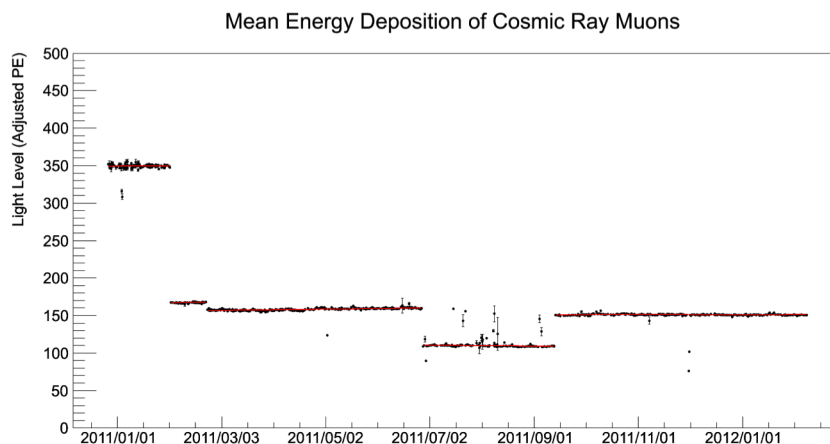
Figure 2.9: The same FEB as in figure 2.8 with red fit lines. The fit lines did well in finding the ranges and closely matching the data.
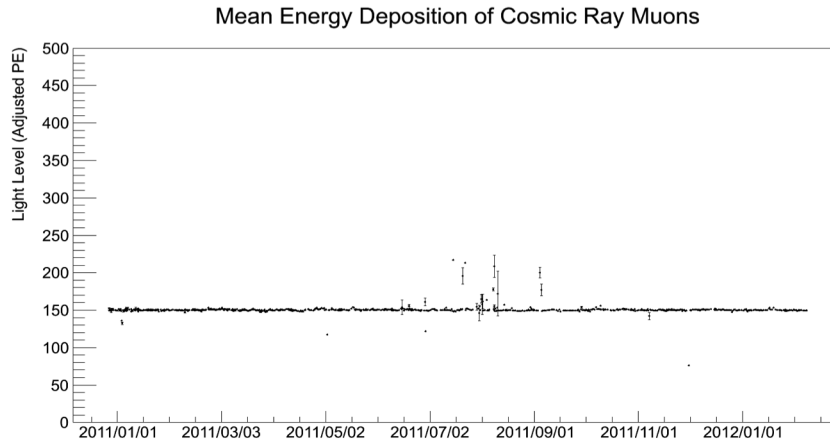
Figure 2.10: The FEB from figure 2.8 with the temporal correction factor applied to each data point. We can now see that our goal of having most of the mean energy deposition constant throughout time is fulfilled.
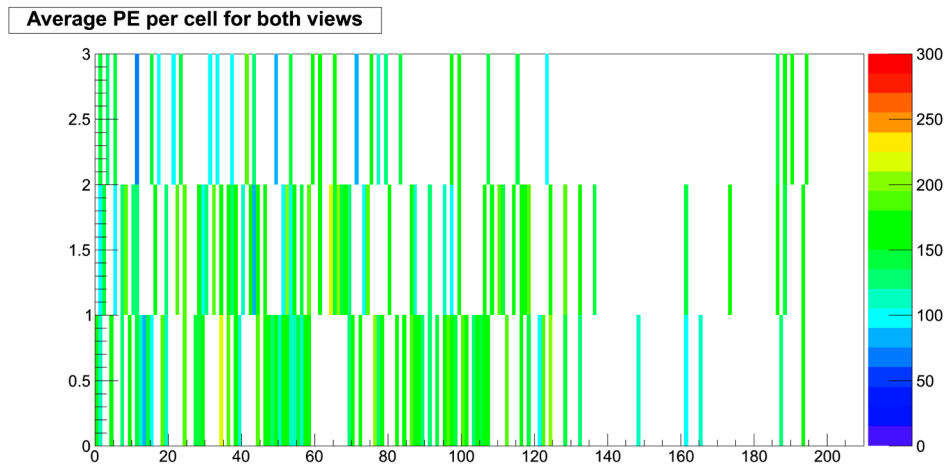
Figure 2.11: This is a representation of the FEBs from both sides of the NDOS. The FEBs in the NDOS show the mean PE counts in Run 12814 (20-21 August 2011). The y-axis is the position of the FEB within the planes of the detector and the x-axis is the position of those planes in the detector. The vertical channels will have 2 FEBs in a plane, and the horizontal channels will have 3 FEBs in a plane. The entire NDOS has a total of 199 planes running from plane 0 to plane 198. The color scaling has the same correspondence to the y-axis of Figures 2.8 - 2.10. So that a 150 adjusted PE in Figure 2.11 is the same 150 PE in this and subsequent figures.
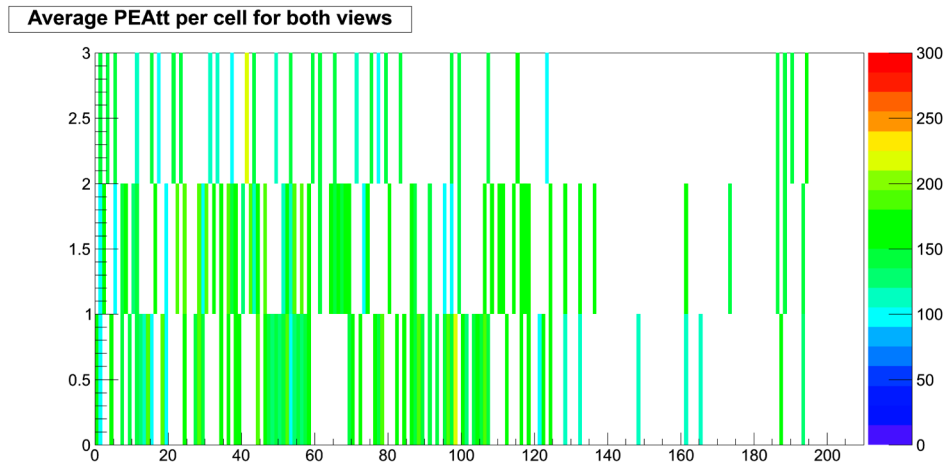
Figure 2.12: The FEBs in the NDOS showing mean PE counts after the spatial response calibration in Run 12814 (20-21 August 2011).
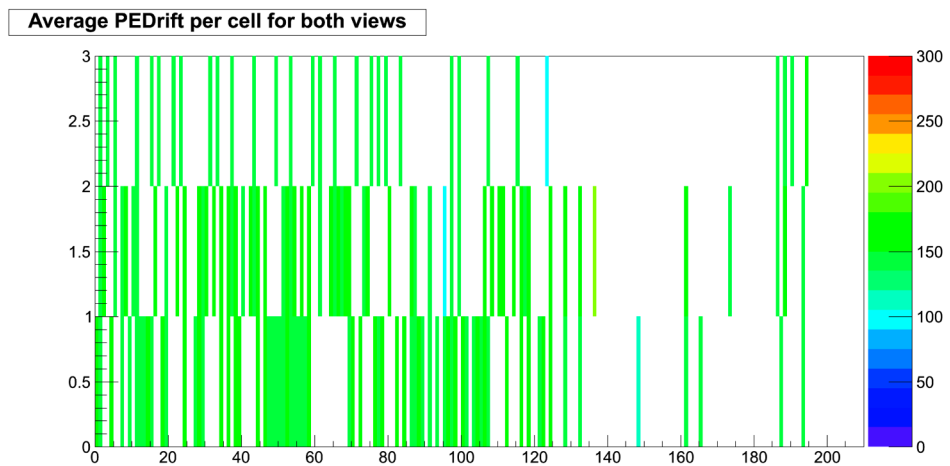
Figure 2.13: The FEBs in the NDOS showing mean PE counts after both spatial and temporal response calibrations in Run 12814 (20-21 August 2011).
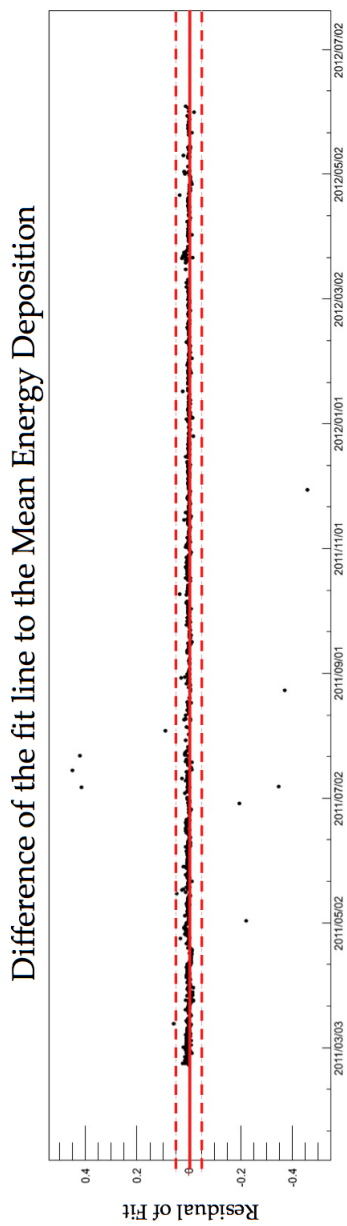
Figure 2.14: This shows the residual of the same FEB as in Figure 2.8 but using recent cosmic data and excluding the threshold and voltage changing periods of time. The solid line indicates a difference of zero percent from the fit line, and the dotted lines represent ±5% difference from the fit line

CHAPTER 3.   The Neutrino Quasi-Elastic Cross-section Measurement

The charged current quasi-elastic neutrino cross-section measurement is important for the interpretation of new neutrino oscillation data, particularly that of NOνA since it lies in the same energy range as the main oscillation measurement. This measurement will help with the understanding of the models used to describe the nucleus of the target material in neutrino experiments, but also the nuclei. The neutrino is an excellent probe into the nuclei, since the neutrino only interacts weakly with particles. The type of model used to describe the nuclei of target material is the Relativistic Fermi Gas model, or RFG model. This model contains a form factor within the general treatment of the weak interactions with nucleons that is unresolved from measurement. This form factor, the axial vector form factor F$_A(Q^2)^†$, is used as the interaction term for when one nucleon changes flavors to another nucleon. It should be noted that the unresolved parameter within the form factor is the effective axial vector mass, M$_A^{eff}$. The equation shown here is the the form factor.

$$F_A(Q^2) = \frac{F_A(0)}{\left(1 + \frac{Q^2}{(M_A^{eff})^2}\right)^2} \tag{3.1}$$

This equation is derived from the simplification of the general treatment from experiments and some assumptions made concerning the form of the factor. $F_A(0)$ is determined from neutron decay experiments, and the form factor utilizes the dipole approximation with a single free parameter [14]. In Figure 3.1 we can see that two groups of experiments measuring the cross section as function of energy are compared to the RFG model with two different M$_A$ parameters. One of the groups is the MiniBooNE and SciBooNE experiments (both using the Booster beam at Fermilab) and the other group being the NOMAD experiment at CERN.

$†$The square of the four-momenta transfer as defined: $Q^2 = -q^2 = -(p_\mu - p_\nu)^2$, where p_μ is the momentum of the out-going muon and p_ν is the momentum of the incident neutrino.

Neutrino experiments measure the cross-section as a function of Q^2 and energy. NOvA in particular will make a measurement using the neutrino beam at 2 GeV which is precisely in the transition region between the two groups of measurements done so far and might help in settling this apparent disagreement.
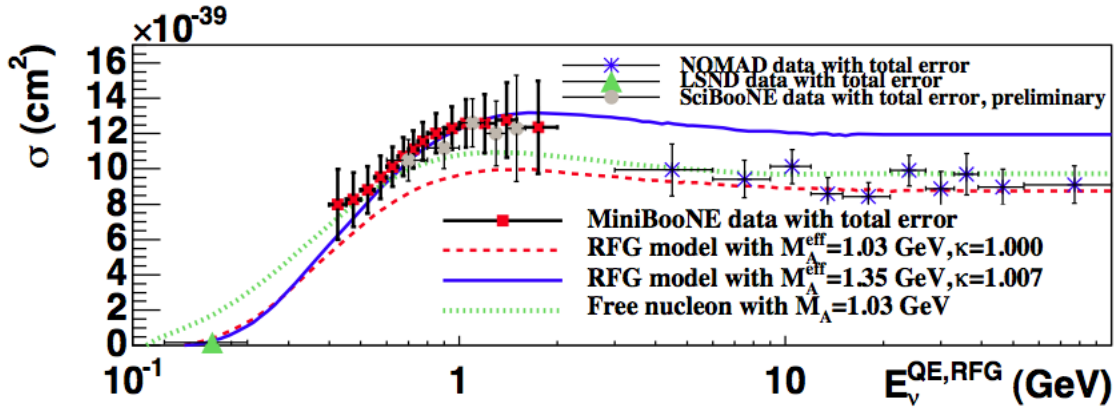
Figure 3.1: This shows the results from 4 different neutrino experiments covering a range of energy for the cross-section measurement using quasi-elastic neutrino interaction. Within this framework, the model of the nucleus is the Relativistic Fermi Gas (RFG) model with a parameter M_A^{eff} as a fitting parameter found from the Q^2 distribution of the interaction. NOνA has the ability to probe the region between MiniBooNE, et.al. and NOMAD to interpret which modeling parameter is correct [15].

3.1 Neutrino Data and Simulation

The data selected in the charged current quasi-elastic cross-section measurement is from the early data collection period of the NuMI beam with NDOS. The data was chosen because it is well understood and used in the development of the analysis. I remind you that in Figure 1.15, we can see the amount of cosmic background that may occur within the data sample. The expected number of cosmic ray muons seen in a neutrino candidate event would be the cosmic rate times the data collection window, $1.7 \times 10^{-3} \mu s^{-1} \times 500 \mu s \approx 1$ cosmic ray muon per spill. More data was collected after significant configuration changes in the detector and is not used in the analysis. The data from this configuration of NDOS corresponds to 443 subruns[†] spanning

[†]One subrun corresponds to approximately 1 hour of data collection in the NDOS.

8 April - 15 May 2011. The NDOS had an exposure of 9.6×10^{18} POT in this period. The number of active APDs during the data collection was about 350 as seen in Figure 1.16.

In this analysis, we use a combination of different simulations to produce and propagate particles from the NuMI beam, to the NDOS, and finally inside the NDOS. To simulate the NuMI beam, we use FLUGG, which is a combination of Fluka and Geant4 [16]. Fluka is responsible for generating the hadrons (e.g. pions and kaons) in the beam, and Geant4 propagates them and interacts the hadrons (i.e. hadron decay) with a target to create the neutrinos for the next simulator. GENIE (Generates Events for Neutrino Interaction Experiments) takes the neutrinos and has them interact within the NDOS [17]. Geant4 then propagates the product particles from the interaction through the detector. The last step is to transport the photons to the APDs in the simulated NDOS for the analysis. The number of POTs used in the Monte Carlo (MC) simulation sample in this analysis is 1.05×10^{21} POTs. The simulated data uses similar channel masking corresponding to the data used in this analysis. The channel masking is the process of determining and removing channels from data that produce high levels of energy deposition continuously in data collection or are not instrumented.

3.2 Data Selection

In this section, I will highlight the importance of each step involved in acquiring the purest sample of quasi-elastic muon neutrino events from the data collected with NDOS. I will discuss in detail the cosmic ray muon background subtraction in order to select only neutrino events from the beam. The importance of discriminant variables will be discussed and how they are used in the separation of quasi-elastic events from other neutrino interaction events. Next I will describe the k-Nearest Neighbor algorithm and how that is used in the analysis. Finally I will report on the results we obtain from using the discriminate variables with cosmic background subtraction.

3.2.1 Cosmic Background Subtraction

The pre-selection cuts are quality cuts applied to a sample of data to remove any background events that can mimic the desired signal events. This process can remove some desired signal

events from the sample, but the idea is to purify the sample to have mostly desired signal events and few background events. The dominant background source is cosmic ray muons and the desired signal events are the neutrino interactions in the NDOS. The quality cuts outlined in this section focus on distinguishing characteristics between neutrino interactions from the beam and cosmic ray muons. These characteristics deal with track angles and start and end points of tracks within NDOS.

The first quality cut ensures that the vertices, or start point, of the neutrino interaction occur within the detector's fiducial volume. This is a volume with dimensions smaller than the NDOS and contained within the detector volume. Figure 3.2 shows the fiducial volume in context of an event display shaded in blue. From the center of the detector, it extends to 115 cm wide and 150 cm high. Along the length of the detector, the fiducial volume starts at 50 cm from the front of the detector going to 770 cm from the front. The fiducial volume cut eliminates any track originating at or beyond the border of the detector. This not only removes cosmic ray muons produced in the atmosphere, but muons made in the surrounding earth, referred to as rock muons, and any interactions that may not be fully contained in the detector itself. It is also important to have the vertex of the interaction within the detector, because we will use the energy surrounding the vertex as an input variable for the k-NN algorithm.

The next cut made on the data is to choose only fully contained interactions. This means that the end points of all reconstructed tracks must be contained inside a defined containment volume. The size of the containment volume has the same dimensions of width and height of the fiducial volume, but allows tracks to end anywhere before 1350 cm from the front of the detector. Figure 3.2 shows the containment volume as an extension of the fiducial volume in context of an event display shaded in blue and red. This ensures that the total energy of the interaction can be calculated correctly. We also require the tracks used in this analysis traverse at least 10 planes in the detector.

Another selection coinciding with the start and endpoints of the reconstructed tracks is a quality cut on the angle of the track with respect to the NuMI beam. This is an effective way of removing a large portion of the cosmic ray muon background events. If a track has a slope of $\left| \frac{z_2 - z_1}{y_2 - y_1} \right| > 1$, then said track can be reasonably assumed to be a cosmic ray muon
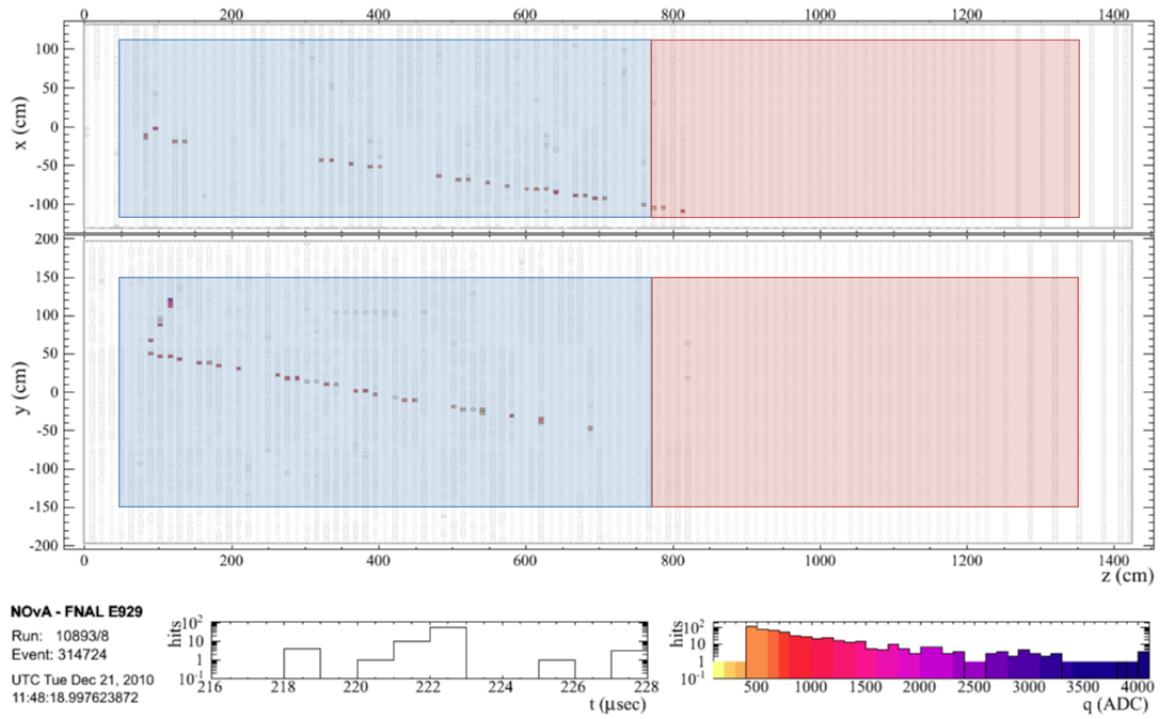
Figure 3.2: This is a neutrino candidate event view in our Event Display. The blue shaded region is the fiducial volume and the red shaded region is the extension of the containment volume from the fiducial volume within our Event Display.

track and is thus cut from the data selection. The slope of 1 makes a $\pm 45°$ angle with respect to the bottom surface of the detector, θ_{NDOS}. In Figrure 1.19 the angle is measured in the $\hat{y}\hat{z}$ plane counterclockwise from the bottom of the detector , which corresponds to -200 cm. The direction of the NuMI beam is $+6.3°$ with respect to the detector. Since this is a small angle, we can approximate the angle of the reconstructed muon track made with respect to the detector is the same as the angle of the reconstructed muon track with respect to the NuMI beam, θ_{NuMI}. We notice that the muon track is traversing the length of the detector. Cosmic ray muons mostly traverse the detector perpendicular to the direction of the NuMI beam.

Figure 1.18 shows the 500 μs time spill window in the NDOS with a peak at 222 μs and a width of 10 μs corresponding to the NuMI beam spill. The reconstructed tracks have passed the fiducial volume quality cut and also traversed the 10 plane minimum requirement. We call any track outside the 10 μs width the out-of-time data (background), and everything within it is now called in-time data (possible signal). We create a distribution of the track angles with respect to the NuMI beam direction for both the out-of-time and in-time data. The out-of-time data has been scaled appropriately to compare between the two sets of data. In Figure 3.3, we show the angular distribution with respect to the NuMI beam of the two sets of data. We first note how well the in-time data matches to the out-of-time data at high angles from the beam line, and an excess can be seen where the muon track angle closely aligns with the beam line. We remove the cosmic ray muon background by subtracting the scaled out-of-time data from the in-time data. From this figure, we can also see that a quality cut of the muon track angle with respect to the NuMI beam line can be made at $cos\theta_{NuMI} = 0.7$, or $\theta_{NuMI} = \pm 45°$, where everything below 0.7 can be considered cosmic background. This would coincide with the slope of the track being less than one and possibly a NuMI beam neutrino event. We can then compare this to neutrino MC, and we see in Figure 3.4, that they match well. The number of events selected through each quality cut is applied. Table 3.1 shows the amount of candidate events removed as quality cuts are applied to remove cosmic ray muons.

The last pre-selection quality cut is the choice of using only events in the NDOS that had one reconstructed neutrino candidate track. Even though in the charged current quasi-elastic interaction there are two tracks, one from the muon and one from the proton, i.e.
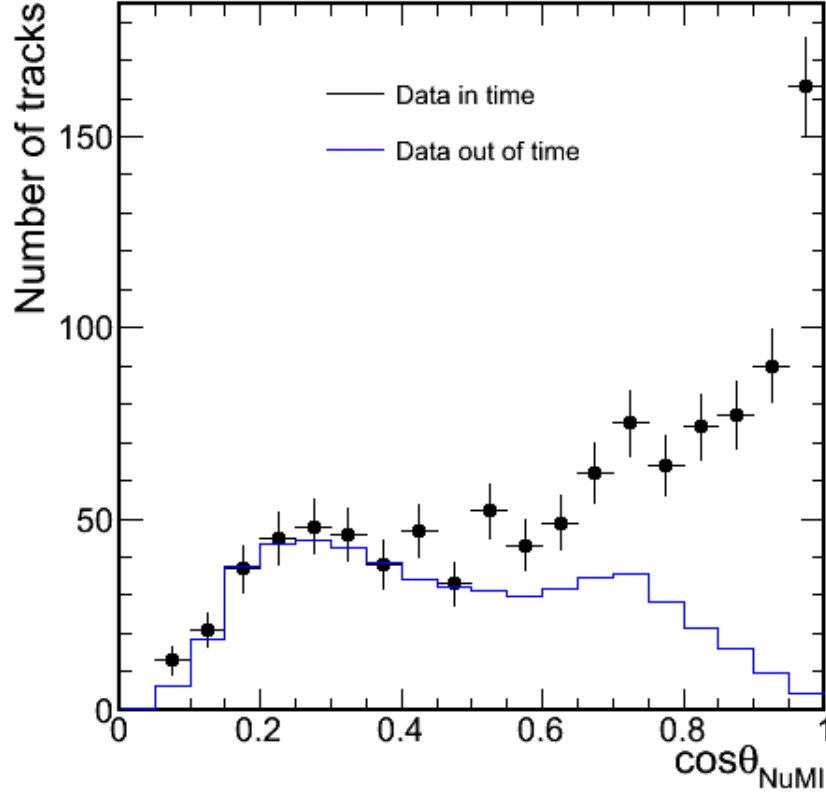
Figure 3.3: The blue line shows the out-of-time data as a function of muon track angle with respect to the NuMI beam line, and the black is the in-time data. The out-of-time data (background) is scaled appropriately for comparison. There is an excess of in-time data aligning with the direction of the NuMI beam, implying these are more likely neutrino interactions from the NuMI beam. The blue line will be subtracted from the black dots in order to remove the background within the 10 μs width [18].

	In-time Data	MC	Out-of-time Data
Starting Sample	24218	134154	1067748
Fiducial and Containment Cut	260	29061	50
Angle Cut	175	27083	23

Table 3.1: A progression of applying the quality cuts to the data and MC and how many candidates are lost at each stage.

$\nu_\mu + n \rightarrow \mu^- + p^+$, this quality cut is made since most of the quasi-elastic interactions have only a single muon track visible [19].
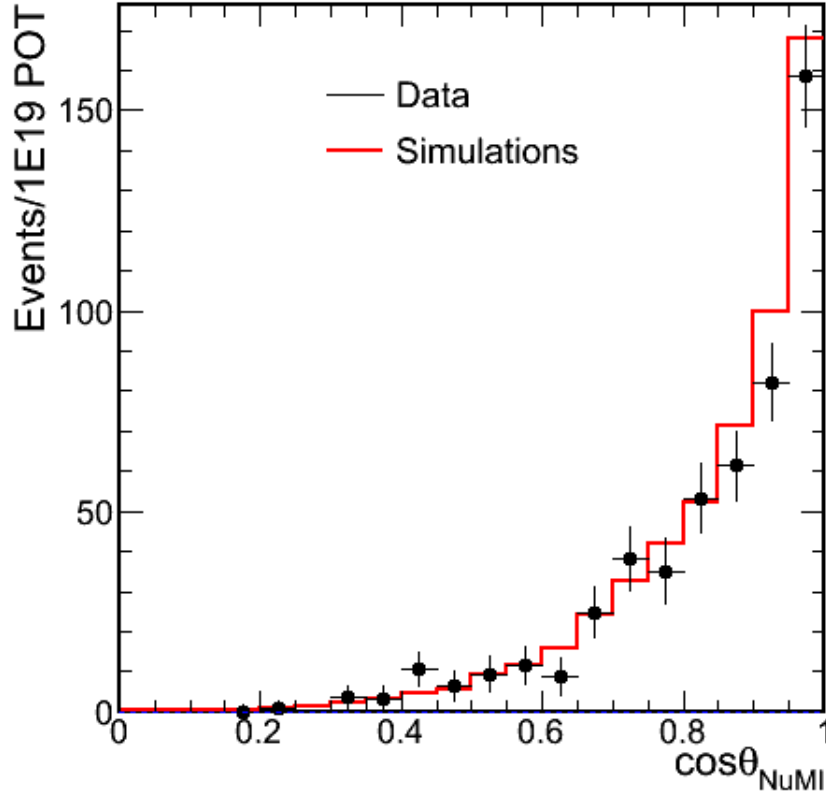
Figure 3.4: The black dots are in-time data points with background subtracted from Figure 3.3. The red line is the Monte Carlo simulation for comparison and seems to agree well with the data [18].

3.2.2   Discriminant Variables for CCQE Signal and Background

In the CCQE analysis, we would like to exclusively use charged current quasi-elastic muon neutrino interactions. The CCQE interaction we are searching for is a neutrino interacting with a neutron and creating a proton and a muon in the final state. Figure 3.5 shows what this topology would look like within the NDOS. Now that we have a pure sample of neutrino candidate events, there are other background interactions to consider. The three background interactions are referred as charged current resonant interactions (CC-RES), charged current

deep-inelastic scattering interactions (CC-DIS), and neutral current interactions (NC). Charged current resonant interactions can simply be described as quasi-elastic interactions with one extra outgoing particle, usually a neutral pion. In Figure 3.6, the resonance topology is shown for the NDOS. Deep-inelastic charged current interactions are interactions with an outgoing charged lepton but also many other particles like charged and neutral pions, neutrons, and protons. The deep-inelastic scattering topology is shown in Figure 3.7. This is the result of the neutrino interacting within the nucleus of an atom with a high enough energy. Neutral current interactions are interactions without an outgoing charged lepton, and Figure 3.8 shows the neutral current topology. Some of the outgoing particles can mimic charged leptons, namely charged pions, in the neutral current interaction and can be confused with signal CCQE events.
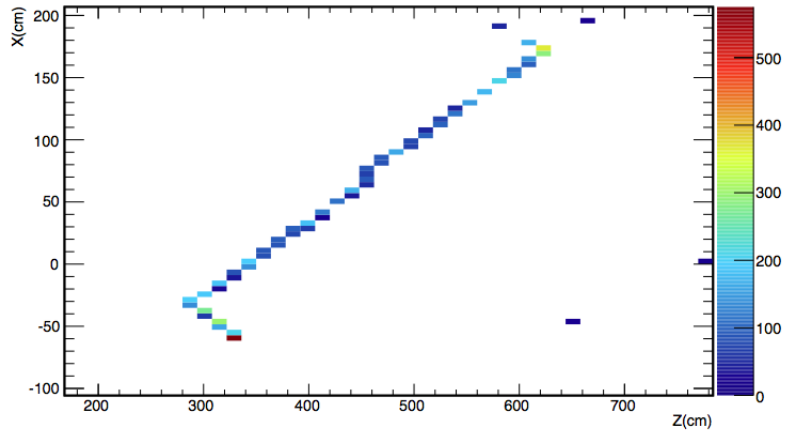

Figure 3.5: This is what a quasi-elastic muon neutrino topology would look like in the NDOS. The primary vertex (i.e. neutrino interaction) begins at about -30 cm in X and 280 in Z. The long nearly uniform energy deposition is the muon coming from the primary vertex, the secondary vertex at the end of the track is the Michel electron coming from the decay of the muon. The shorter track coming from the primary vertex is the proton. The dark red end point is the Bragg peak of the proton stopping in the detector. The other dark blue pixels are simulated noise in the detector.

The input variables that were finally selected to represent the space to discriminate signal and background events are: the number of planes the single track traverses in the detector, the total amount of energy around the vertex of the interaction, and the mean energy deposition per a plane of the single traversing particle. These variables were chosen as discriminants for
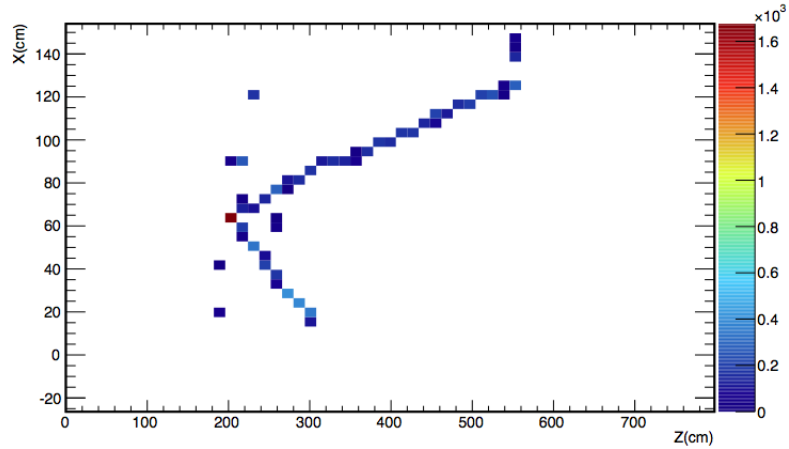
Figure 3.6: This is what a resonance muon neutrino topology would look like in the NDOS. The primary vertex begins at about +60 cm in X and 200 cm in Z. The tracks seen coming from the vertex are a long muon track with a proton not moving far from the vertex indicated by the red vertex point, and the photons from a decayed neutral pion. They are probably overlapping in the X-Z plane.
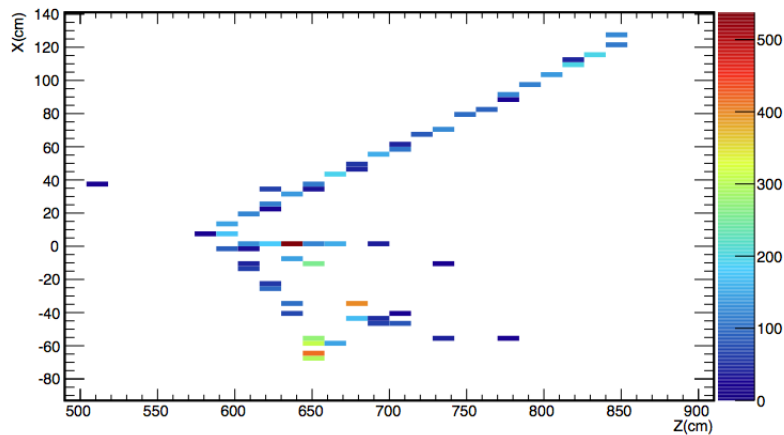

Figure 3.7: This is what a deep-inelastic scattering muon neutrino topology would look like in the NDOS. The primary vertex starting at about +10 cm in X and 570 cm in Z. The muon can be quickly identified by the long track with nearly constant energy deposition, but the other tracks are product hadrons (e.g. neutral or charged pions, protons, etc.) from the interaction.
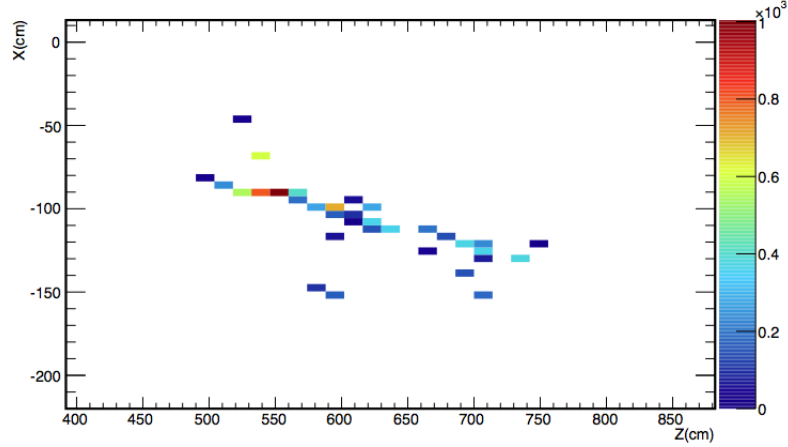
Figure 3.8: This is what a neutral current topology would look like in the NDOS. Similar to Figure 3.7 but without the muon track.

the three types of background interactions.

The number of planes the single track traversed in the detector can do well distinguishing neutral current and deep-inelastic scattering charged current interactions from the charged current resonant and quasi-elastic interactions, as seen in Figure 3.9. The total energy around the vertex has good separation between charged current resonant interactions from the charged current quasi-elastic interactions, as seen in Figure 3.10. Finally, the mean energy deposition of the reconstructed track per plane has some resolving power between the quasi-elastic interactions with charged current resonant and deep-inelastic scattering interactions, but even better power against the neutral current interactions, see Figure 3.11.

By taking these three input variables and grouping the CC-RES, CC-DIS, and NC into the background category, we can use the discriminant powers of each input variable into a multi-variate analysis. We use the k-Nearest Neighbor (k-NN) algorithm as a multi-variate algorithm by combining the variables and using it to separate the signal and background in our data sample.
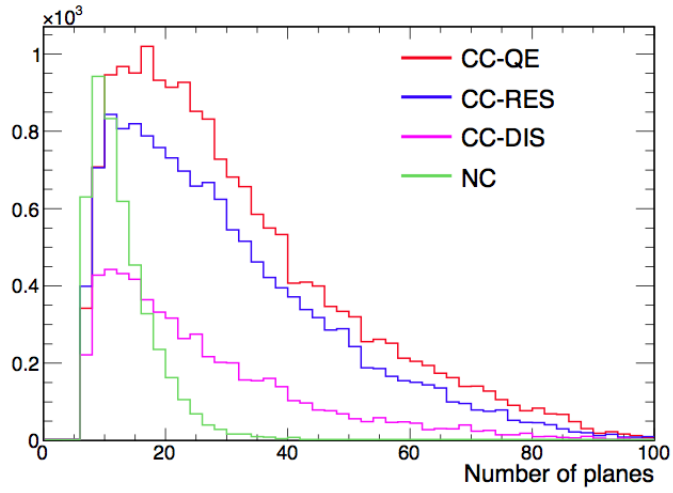
Figure 3.9: This is the number of interactions as a function of the number of planes the muon track traversed in the NDOS. The background is separated to show contribution of the different event topologies discussed in this section.
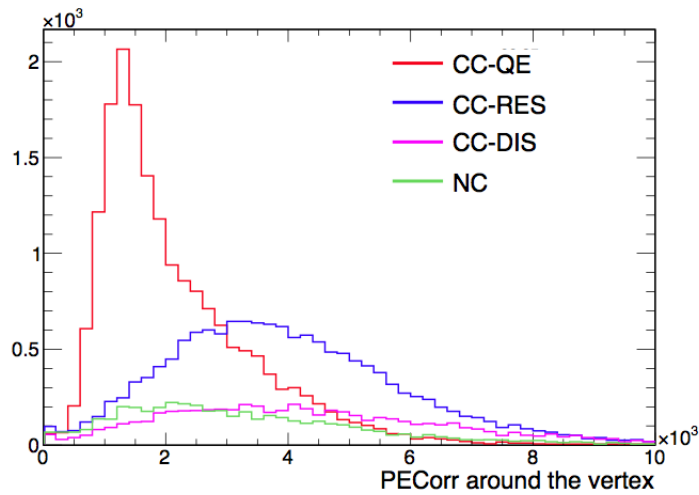

Figure 3.10: This is the number of interactions as a function of the amount of energy deposition around the vertex of the neutrino interaction.
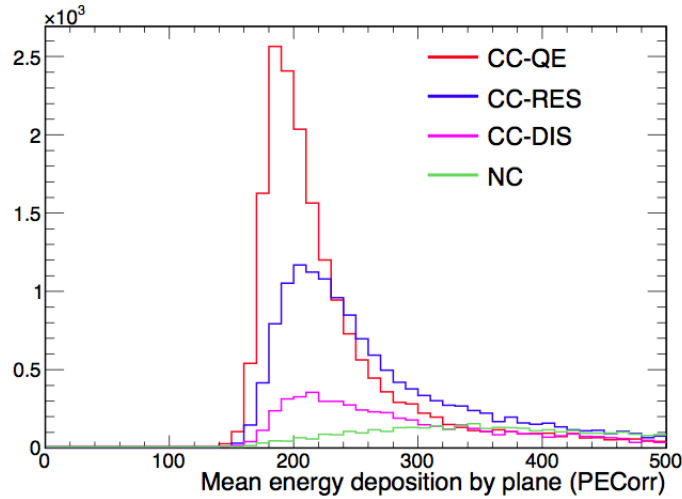
Figure 3.11: This is the number of interactions as a function of the average energy deposition of the muon track in each plane it traverses in NDOS.

3.2.3 The k-NN Algorithm

The k-NN is a method of taking discrete points within a multidimensional variable space, and creating a probability density function to determine the likelihood of another point being signal or background. This method takes a sample of points, a training sample, with known binomial signal or background value (e.g. a point that is signal will have a value of 1, whereas a background point will have a value of 0). Each point's coordinates within the space have been generated from the same reconstruction method that data (points with unknown signal/background value) will use.

Once the training sample has been distributed throughout the space defined by the variables, test points are created to search for k events close to it. In this analysis, we use a k value of 100. This is the number of events selected in a test points neighborhood to decide if the test point will be a signal or background-like event. The closeness of a signal or background event is determined by some distance metric. We use a rescaled Euclidean distance or

$$R_{rescaled} = \left(\sum_{i=1}^{n_{var}} \frac{1}{w_i^2} |x_i - y_i|^2 \right)^{\frac{1}{2}} \tag{3.2}$$

Where x_i the coordinate of the test point and y_i is the coordinate of each nearest neighbors, w_i is the width of each variable distribution or weight factor, and n_{var} is the number of input

variables used (e.g. $n_{var} = 3$ in our case). We use this metric to ensure points are not artificially separated by different scales used in the input variables. To prevent this skewing, a weight factor is calculated. This weight factor applied to each variable and is found from the width of the distribution (80% of the training events) for that variable with both signal and background events combined. The purpose of the k-NN method is to compute a relative probability of how likely a point is to be signal using the 100 nearest neighbors. To calculate this probability, P_S we use:

$$P_S = \frac{k_S}{k_S + k_B} \tag{3.3}$$

where k_S is the number of signal-like neighbors and k_B is the number of background-like neighbors. In Figure 3.12, the k-NN output of the relative probability that each MC event is either a signal or background event. In this distribution the value of 1 is a signal event and 0 is a background event. Looking at Figure 3.13, we choose any k-NN output value greater than 0.3 as a quasi-elastic muon neutrino candidate, because the significance in signal over square root signal plus background is the greatest at this point.
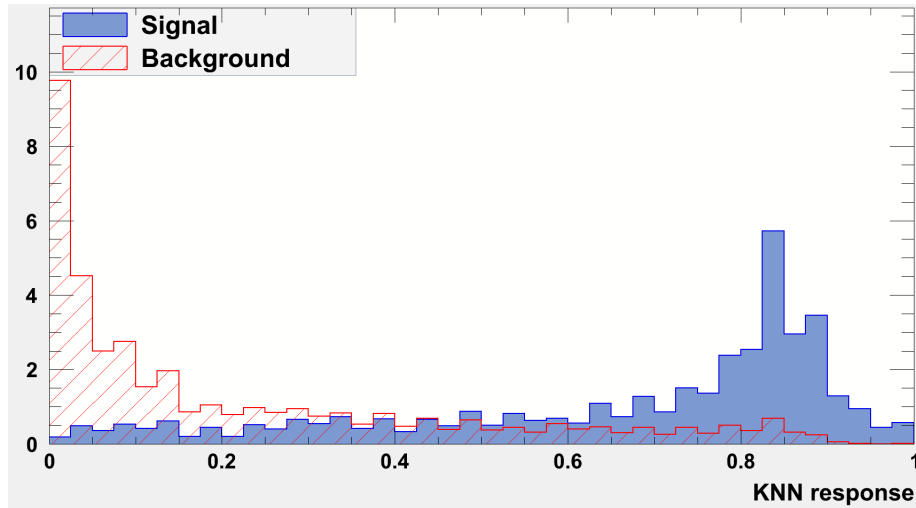

Figure 3.12: This is the k-NN output for the training MC sample. The signal in blue, has most of its testing points close to 1 indicating it signal like, and defining where in the three variable space the signal will most likely be. The background in the red striping is highly separated from the signal events. Most of these events are at or very near 0, indicating it is a background event.
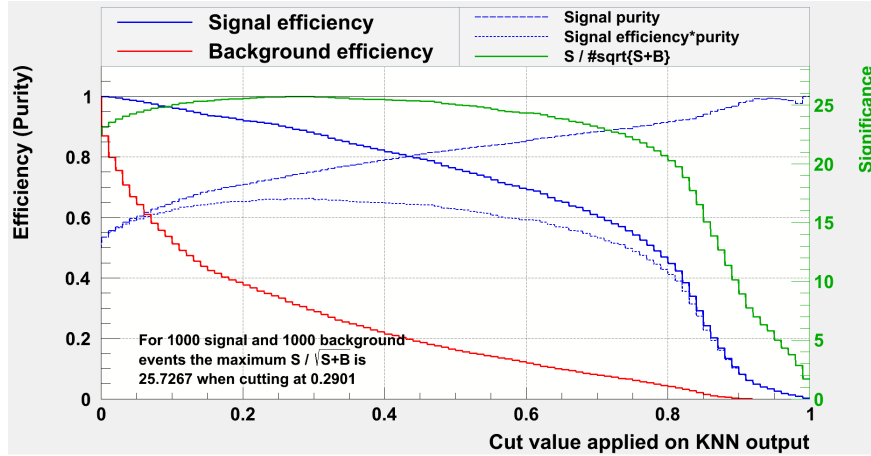
Figure 3.13: This shows the cut efficiencies and where the optimal cut would be to separate signal from background. The best place to cut the background would be where the significance is maximal. In this case, the maximum point in the significance is approximately 0.3 kNN output value.

3.3   Results

In Figures 3.14, 3.15, and 3.16 we show each of the input variables for cosmic ray background subtracted data and neutrino MC. The MC contains CCQE at the default value for the $M^{e}ff_{A}$ parameter in the MC and the 3 background categories discussed before. Figure 3.17 shows these distributions for the k-NN variable. A total of 90 events are considered after all preselection cuts and 58 remain after a cut of 0.3 in this variable. The 32 data points below 0.3 will be considered background events (the resonance and deep-inelastic charged currents and neutral current interactions), where the rest will be considered the signal (quasi-elastic muon neutrino candidates) for the cross-section measurement.
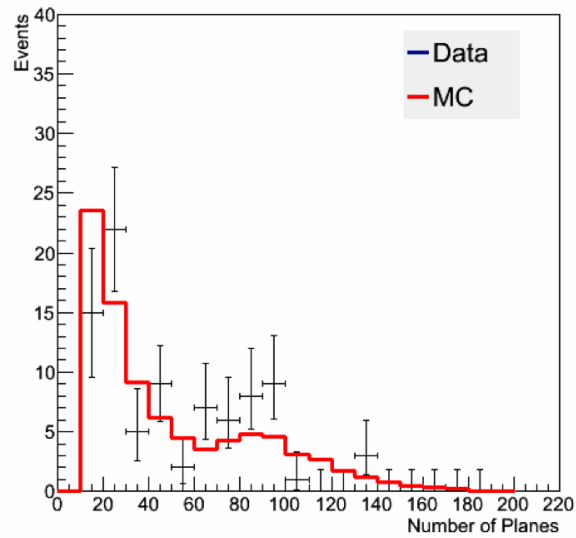
Figure 3.14: This is the background subtracted data (black) and MC (red) event distribution for the input variable: number of planes the muon track traversed. The MC is area normalized to the data for this comparison.
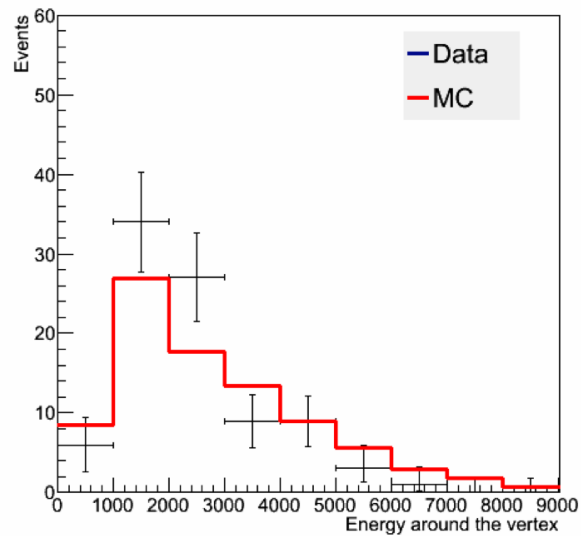
Figure 3.15: This is the background subtracted data (black) and MC (red) event distribution for the input variable: energy deposition around the neutrino interaction vertex. The MC is area normalized to the data for this comparison.
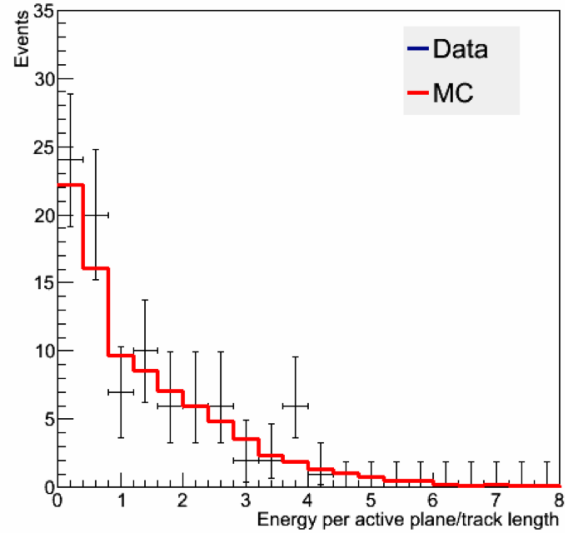
Figure 3.16: This is the background subtracted data (black) and MC (red) event distribution for the input variable: mean energy deposition per active plane for every muon track. The MC is area normalized to the data for this comparison.

Figure 3.17: This is the k-NN output from the background subtracted data (black) input variables and the MC (red). Any event above the value of 0.3 kNN is considered a quasi-elastic muon neutrino candidate. The MC is area normalized to the data for this comparison.

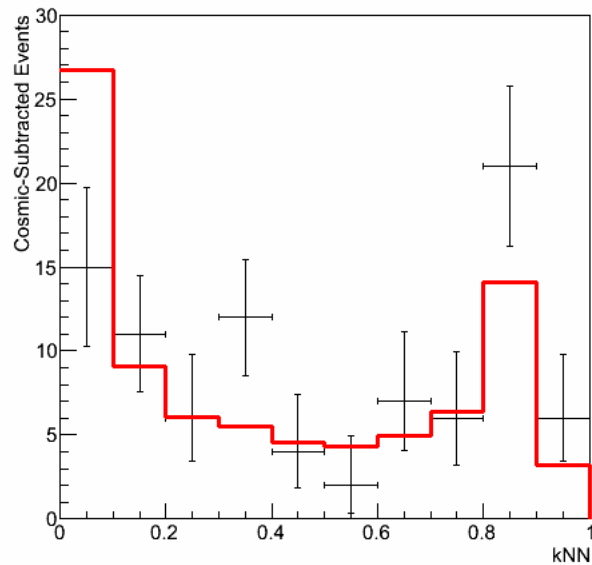# CHAPTER 4. Calibration Effects for the Quasi-Elastic Cross-Section Measurement

In order to make the charged current quasi-elastic (CCQE) cross-section measurement a selection algorithm for this type of events has been developed [20]. The algorithm is based on the k-Nearest Neighbor (k-NN) algorithm which uses several variables to separate signal events (quasi-elastic muon neutrino candidates) from background events in a data sample. The input variables are related to reconstructed track quantities such as the length of the muon track. The calibration will be subject to uncertainties which might impact these variables and subsequently the signal selection efficiency. I have studied these calibration effects within the CCQE measurement that is being done with data collected from the NDOS. In the following sections, I will describe the neutrino data and simulations from the NDOS, the data selection, the spatial and temporal calibrations applied in the CCQE analysis, and finally the uncertainty that arises from these calibrations in the CCQE analysis. In the data selection portion, I will discuss in detail the pre-selection and background subtraction, the discriminant input variables, and the k-NN algorithm.

4.1 Detector Response Calibration for the CCQE Analysis

We expect that variations in detector response can have an impact in the physics quantities used to do the data selection for the quasi-elastic cross section measurement. We can study the impact by calculating the input variables as well as k-NN probability using the uncalibrated energy deposition and observing the change when the spatial and temporal detector response calibrations are applied. Figure 4.1, 4.2, 4.3, and 4.4 show the effects of each of these stages. There is no effect in the variable related to number of planes, since the variable itself and the

steps in the reconstruction do not depend on energy. For the other variables the effects are mostly outside of the signal region and thus it has a small impact on the number of events selected. When the input variables and the k-NN output are compared to the Monte Carlo, as it can be seen in Figure 4.1, 4.2, 4.3, and 4.4 that the calibration does indeed bring the data closer to the prediction. The correction from the temporal detector response is small because, as it was shown in section 2.3, the changes in the detector response were restricted to a few channels during the data taking period.
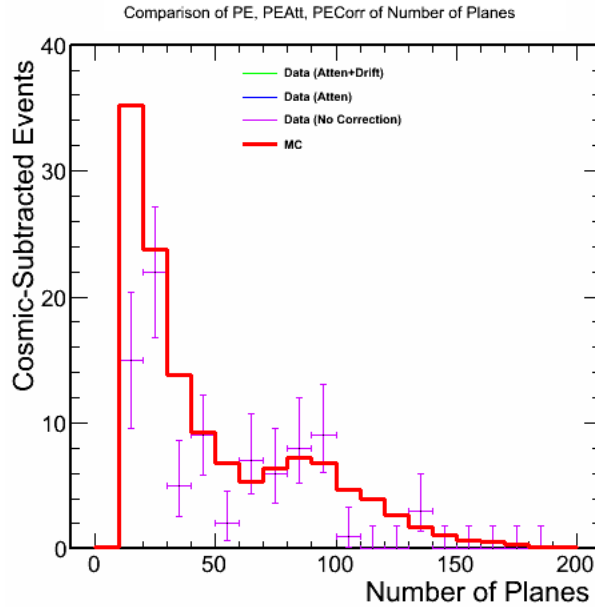
Figure 4.1: This is a comparison of the input variable for the number of planes traversed in the NDOS from the muon track between temporal and spatial calibrations. The violet, blue, and green points with error bars are the data and the red line is the MC for comparison. The violet data set is data without any response calibration applied to the recorded energy deposition in the detector. The blue data set is data with only the spatial response calibration applied to the recorded energy deposition in the detector. The green data set is data that has both spatial and temporal response calibrations applied to the recorded energy deposition in the detector. For this variable, the number of planes a muon traverses in the detector is not dependent on the detector response and does not change when any of the response calibrations are applied. The MC is area normalized to the data for this comparison.
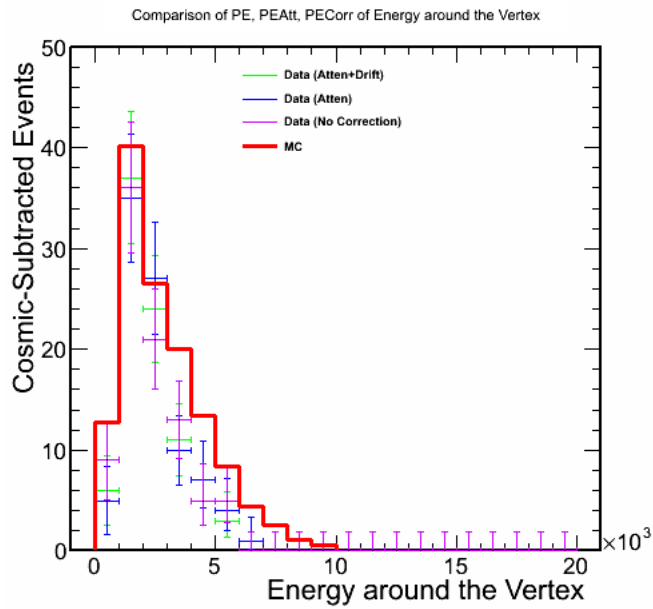
Figure 4.2: This is a comparison of the input variable for the energy deposition around the neutrino interaction vertex between temporal and spatial calibrations. The violet, blue, and green points with error bars are the data and the red line is the MC for comparison. The violet data set is data without any response calibration applied to the recorded energy deposition in the detector. The blue data set is data with only the spatial response calibration applied to the recorded energy deposition in the detector. The green data set is data that has both spatial and temporal response calibrations applied to the recorded energy deposition in the detector. The MC is area normalized to the data for this comparison.

Figure 4.3: This is a comparison of the input variable for the mean energy deposition per active plane for every muon track between temporal and spatial calibrations. The violet, blue, and green points with error bars are the data and the red line is the MC for comparison. The violet data set is data without any response calibration applied to the recorded energy deposition in the detector. The blue data set is data with only the spatial response calibration applied to the recorded energy deposition in the detector. The green data set is data that has both spatial and temporal response calibrations applied to the recorded energy deposition in the detector. The MC is area normalized to the data for this comparison.
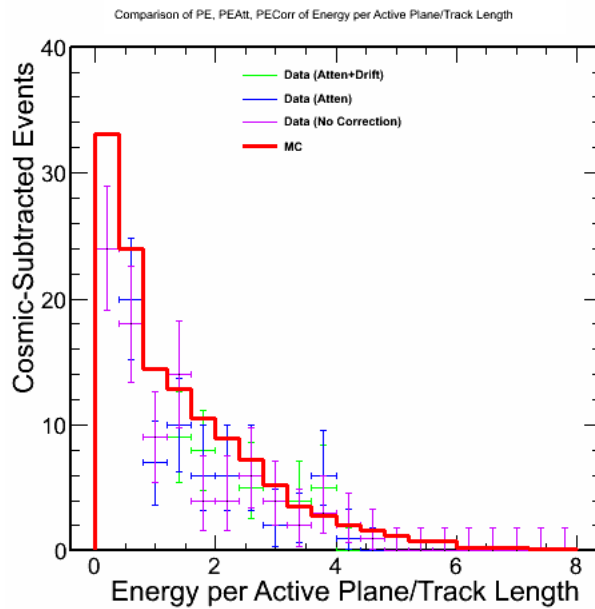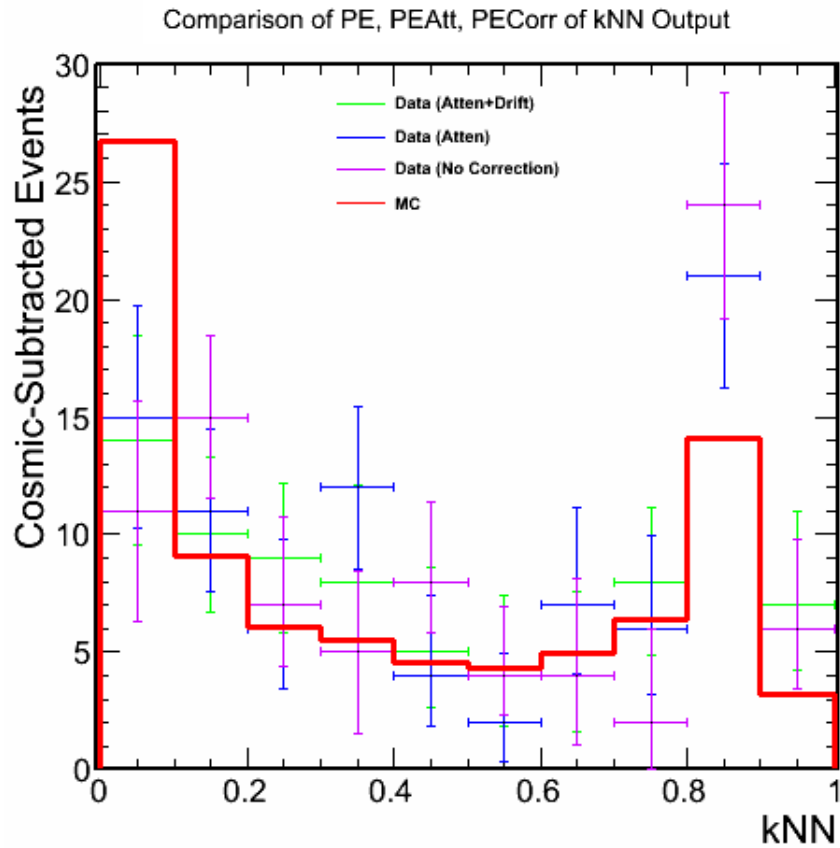
Figure 4.4: This is a comparison of the k-NN output between temporal and spatial calibrations. The violet, blue, and green points with error bars are the data and the red line is the MC for comparison. The violet data set is data without any response calibration applied to the recorded energy deposition in the detector. The blue data set is data with only the spatial response calibration applied to the recorded energy deposition in the detector. The green data set is data that has both spatial and temporal response calibrations applied to the recorded energy deposition in the detector. Any value greater than 0.3 in the k-NN output is considered signal. The MC is area normalized to the data for this comparison.

4.2 Calibration Uncertainty for the CCQE Analysis

In order to compare the MC and the data results accurately, we must normalize the two samples to the exposure time of the detectors to the neutrino beam. The MC will use higher statistics in order to predict our expected data results with minimal statistical uncertainty. We use more simulated beam spills (the POTs) in order to accomplish this. In previous sections we have used area normalization in the comparison of input variables and k-NN output of the MC and data in order to better understand the calibration and particle ID performances. In this section we use POT normalization.

We can now estimate the overall detector response uncertainty for the CCQE analysis by using the neutrino Monte Carlo. In order to do that we will take an overall shift of the energy deposition by factors of $\pm 2.5\%$, $\pm 5\%$ and $\pm 10\%$. This is a worse case scenario uncertainty that assumes that for all events the energy deposition is biased in the same direction. When this shift is taken the input variables of the total vertex energy and the energy per active plane change. However, the shift does not change the input variable of number of planes the longest track traversed in the detector, since this variable is energy independent. The k-NN output variable is then calculated for each data and Monte Carlo event with the new overall detector response shift. The events with a k-NN value of greater than 0.3 are counted. The number of selected events using these shifts can be seen in Table 4.1. The variation of events in the data are within the statistical errors of the sample and thus we use the Monte Carlo to calculate the detector response systematic uncertainty.

Percent Shift	-10%	-5%	-2.5%	0%	+2.5%	+5%	+10%
Monte Carlo (# events)	74.6	70.3	68.1	*66.0*	63.9	62.0	58.0
Data (# events)	60.2	58.1	55.5	*53.8*[†]	52.0	51.3	45.9

Table 4.1: Effect of shifting the drift and attenuated corrected PE in the input variables to the kNN by an overall percent factor. [†]The number of quasi-elastic muon neutrino interactions tabulated without drift calibration is 54.1 events. The Monte Carlo should not change since it is not affected by drifting.

In Section 2.3.3, we considered that 98% of the runs could be within $\pm 5\%$ variations, so

we can consider this to be a reasonable systematic shift. Figure 4.5 shows the resulting k-NN distributions of the data and the MC with statistical and systematic uncertainties respectively. These distributions are POT normalized as they will be in the final measurement. In the signal region the MC is in excellent agreement with the data. The overall number of MC events selected is slightly above that of the data but within the combined statistical and systematic uncertainty. The lowest bin where the Monte Carlo is significantly higher than the data is expected to contain a very minimal amount of signal. This discrepancy is being investigated. The analysis is still under development and many of the uncertainties, such as the neutrino beam flux, are still being studied.

The results we obtain are: $66.0^{+4.3}_{-4.0}$(syst.)± 0.7(stat.) events and 53.8 ± 9.2(stat.) events in data. Thus the systematic error for the detector response calibration is much smaller than the current statistical error on the data, and so it is a minor systematic uncertainty. In the future much more data will be available in the Near Detector. A few months of Near Detector data will be approximately 8 times more data than it is used in this analysis. The statistical error of that data will be comparable with the 2.5% detector response variation. Thus more effort must be done in reducing the detector response systematic error. This can be achieved by considering the smaller variation and moving away from the worse case scenario used here and by evaluating each of the components of the detector response individually.
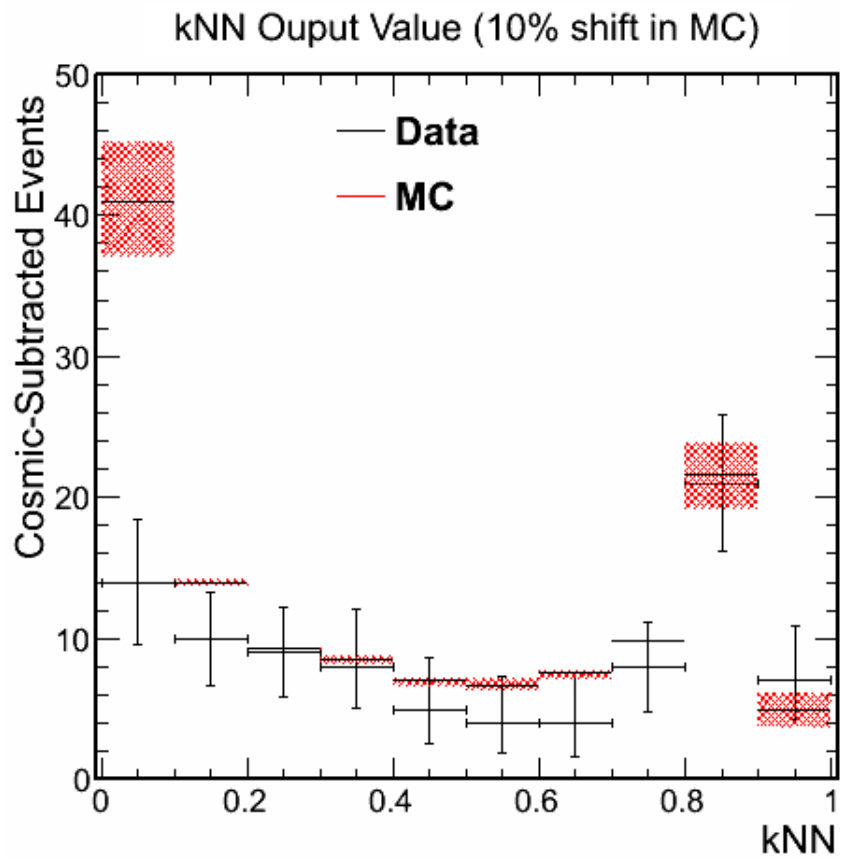
Figure 4.5: This is the POT normalized k-NN output from the background subtracted data (black) input variables and the $\pm 5\%$ shift on MC (red shading). Any event above the value of 0.3 kNN is considered a quasi-elastic muon neutrino candidate.

CHAPTER 5.   Conclusions

The NDOS was built in order to demonstrate many aspects of constructing and performing a long-baseline neutrino experiment. With it we have demonstrated that the physics goals that the NOνA collaboration has laid out can be accomplished. The construction of a working prototype shows the scalability of the technology that will be used in the NOνA Near and Far Detectors. Also, the tools we developed in the commissioning and calibration of the NDOS, will greatly aid in the Near and Far Detector commissioning and performance monitoring. The combined efforts in simulation and reconstruction for the physics analyses using beam neutrinos that have been developed show that we are taking steps and contributing to the achievement of those goals.

The detector response calibration we have developed and implemented in the NDOS has laid the foundation for use in the NOνA Near and Far Detectors. These have been shown to perform well in the NDOS, but the detector response calibration will need more improvements as we move to higher statistics analyses at the Near and Far Detectors. The contribution of the drift point calibration in the NDOS have helped to the commissioning of NDOS and provided the means of monitoring the stability of the data collected over time.

The NDOS has shown that with this technology, we can observe neutrino interactions and develop analyses with this data. The CCQE cross-section measurement is one of these analyses. This analysis will help to shed light onto the discrepancy between experiments surrounding the nucleon model used to interpret the CCQE measurement. With the NDOS data that has been collected, we have shown that the systematic uncertainty of the detector response calibration is not significant to the CCQE measurement. Once the Near Detector is collecting data, we will not only be ready to improve this analysis but the uncertainties that come from the calibrations discussed here.

BIBLIOGRAPHY

[1] R. Zwaska et al. Beam-based Alignment of the NuMI Target Station Component at FNAL. *Nucl. Instr. Meth.*, 568:548–560, 2006.

[2] G. Feldman et al. NOνA Technical Design Review. Technical report, Fermi National Accelerator Laboratory, 2007.

[3] S. Kopp et al. Secondary Beam Monitors for the NuMI Facility at FNAL. *Nucl. Instr. Meth.*, 568:503–519, 2006.

[4] J. Beringer, 2012. Phys. Rev. D86, 010001.

[5] L. Corwin. NuMI Beam Simulations: Update on FLUGG and joint NuMI Beam Group. NOVA-docdb-6959-v1, January 2012. Internal Document.

[6] J. Paley. NDOS Operations Summary. NOVA-docdb-7327-v1, April 2012. Internal Document.

[7] G. S. Davies. Cosmic Rate Plots for Blessing. NOVA-docdb-7207-v2, March 2012. Internal Document.

[8] G. S. Davies. Performance of the CosmicTrack Algorithm. NOVA-docdb-7230-v2, March 2012. Internal Document.

[9] R. B. Patterson(for NOνA Collaboration). The NOνA Experiment: Status and Outlook. The proceedings of the XXV International Conference on Neutrino Physics and Astrophysics (Neutrino 2012), 2012.

[10] C. Backhouse. Calibration Technote. NOVA-docdb-7410-v1, May 2012. Internal Document.

[11] M. Messier, 2011. Private Communication.

[12] R. B. Patterson, 2011. Private Communication.

[13] C. B. Smith. *Calibration of the MINOS Detectors and Extraction of Neutrino Oscillation Parameters.* PhD thesis, University College London, 2002.

[14] M. E. Dorman. *Cross Section Measurements for Quasi-Elastic Neutrino-Nucleus Scattering with the MINOS Near Detector.* PhD thesis, University College London, 2008.

[15] M. O. Wascko. Recent Measurements of Neutrino-Nucleus Quasi-Elastic Scattering. *Nuclear Physics B Proceedings Supplement*, 00:1–5, 2011.

[16] M. Campanella et al. Reusing code from fluka and geant4 geometry. ALT-SOFT 98-039, CERN, 1998.

[17] C. Andreopoulos et al. The GENIE Neutrino Monte Carlo Generator. *Nucl. Instrum. Meth.*, A614:87–104, 2010.

[18] M. Betancourt. NDOS Data and QE Studies. NOVA-docdb-6918-v1, January 2012. Internal Document.

[19] M. Betancourt. Blessed Plots for NuMI Beam Data. NOVA-docdb-7206-v2, March 2012. Internal Document.

[20] M. Betancourt. QE Studies Update. NOVA-docdb-7296-v1, April 2012. Internal Document.